Deep Learning Reveals Endogenous Sterols as Allosteric Modulators of the GPCR-Gα Interface

Sanjay Kumar Mohanty[1,†], Aayushi Mittal[1,†], Namra[3,4,†], Aakash Gaur[2,3], Subhadeep Duari[1], Saveena Solanki[1], Anmol Kumar Sharma[1], Sakshi Arora[1], Suvendu Kumar[1], Vishakha Gautam[1], Nilesh Kumar Dixit[1], Karthika Subramanian[1], Tarini Shankar Ghosh[1], Debarka Sengupta[1,5], Shashi Kumar Gupta[2,3], Natarajan Arul Murugan[1], Deepak Sharma[3,4,#] and Gaurav Ahuja[1,5,#]

[1]Department of Computational Biology, Indraprastha Institute of Information Technology-Delhi (IIIT-Delhi), Okhla, Phase III, New Delhi, 110020, India.
[2]Pharmacology Division, CSIR-Central Drug Research Institute, Lucknow, India
[3]Academy of Scientific and Innovative Research (AcSIR), Ghaziabad, India.
[4]CSIR-Institute of Microbial Technology, Sector-39A, Chandigarh -160036, India
[5]Infosys Centre for AI, Indraprastha Institute of Information Technology-Delhi (IIIT-Delhi), Okhla, Phase III, New Delhi, 110020, India.

[†]Equal contributions

Correspondence:
Gaurav Ahuja; Email: gaurav.ahuja@iiitd.ac.in
Deepak Sharma; Email: deepaks@imtech.res.in

Running title: Modulation of GPCR-Gα binding via intracellular metabolites

Author Contributions: The study was conceived by G.A. Computational analysis workflows were designed by G.A. Statistical guidance was provided by D.S. Docking, and Molecular Simulations were supervised by N.A.M and conducted by N.A.M, and S.K.M. Data analyses was performed by S.K.M., A.M., S.S., S.K., S.D., A.K.S., S.A., V.G., T.S.G., N.K.D and K.S.. S.K.M built the Gcoupler Python package. G.A. and A.M. designed yeast experimental workflows and performed by A.M. Site-directed yeast mutants were created by N. and D.S. Human cell culture-based experiments were performed and analyzed by A.G., and S.K.G. Illustrations were drafted by A.M., S.K.M., and G.A. G.A. wrote the paper. All authors have read and approved the manuscript.

Competing Interest: The authors declare that they have no competing interests.

Classification: Biological Sciences/Biophysics and Computational Biology

Keywords: Programmed Cell Death, Deep Learning, GPCR, Hypertrophy, Mating, Yeast

ABSTRACT

Endogenous intracellular allosteric modulators of GPCRs remain largely unexplored, with limited binding and phenotype data available. This gap arises from the lack of robust computational methods for unbiased cavity identification, cavity-specific ligand design, synthesis, and validation across GPCR topology. Here, we developed Gcoupler, an AI-driven generalized computational toolkit that leverages an integrative approach combining *de novo* ligand design, statistical methods, Graph Neural Networks, and Bioactivity-based ligand prioritization for rationally predicting high-affinity ligands. Using Gcoupler, we interrogated intracellular metabolites that target and regulate the GPCR-Gα interface (Ste2p-Gpa1p), affecting pheromone-induced programmed cell death in yeast. Our computational analysis, complemented by experimental validations, including genetic screening, multi-omics, site-directed mutagenesis, biochemical assays, and physiological readouts, identified endogenous hydrophobic metabolites, notably sterols, as direct intracellular allosteric modulators of Ste2p. Molecular simulations coupled with biochemical signaling assessment in site-directed Ste2p mutants further confirmed metabolites binding to GPCR-Gα obstruct downstream signaling, possibly via cohesive effect. Finally, by utilizing isoproterenol-induced, GPCR-mediated human and neonatal rat cardiac hypertrophy models, we observed elevated metabolite levels attenuate hypertrophic response, reinforcing the evolutionary relevance of this mechanism.

INTRODUCTION

G protein-coupled receptors (GPCRs) are critical regulators of cellular processes and thus represent prime drug targets (1–3). While traditional GPCR-targeted therapies focus on orthosteric sites, recent advances have revealed allosteric sites offering novel therapeutic avenues (4, 5)(5–7). Although exogenous synthetic allosteric modulators are known, endogenous counterparts remain poorly characterized (8–13). Developing high-affinity endogenous modulators requires integrating structure-based design, artificial intelligence (AI), and assays, yet traditional approaches like SAR analysis are hampered by limited GPCR allosteric modulator data (14, 15). While experimental techniques like FRET and BRET can validate allosteric compounds, their use in high-throughput screening for novel intracellular modulators is challenging (16–18). Identifying endogenous GPCR allosteric modulators is further complicated by factors like incomplete GPCR topology data (19) and vast chemical space (1, 20). This necessitates a hybrid computational approach combining allosteric site prediction, *de novo* ligand synthesis, and efficient screening, potentially enhanced by AI. Existing *de novo* drug design tools often lack practical applicability for this purpose due to computational limitations and high technical demands (21–27).

To overcome these challenges, we developed Gcoupler, a software suite (available as a Python package and Docker image) that integrates structural biology, statistical methods, and deep learning to identify GPCR allosteric modulators. We demonstrated the usability and applicability of Gcoupler in identifying novel endogenous modulators of GPCRs by exploiting the α-pheromone (α-factor)-induced mating or programmed cell death (PCD) pathway of *S. cerevisiae*. Notably, it is well documented that the highly elevated, non-physiological levels of α-factor trigger PCD in less than half of the MATa population (28). Moreover, an equivalent concentration of α-factor triggers distinct PCD kinetics across distinct laboratory strains; for example, BY4741 is more resistant than the W303 strain (29). We, therefore, hypothesized that a subset of pheromone-resistant cells might regulate the Ste2p-mediated PCD signaling via the endogenous intracellular metabolites by operating at the Ste2-Gα binding interface. Using Gcoupler, we identified a subset of intracellular metabolites that could potentially bind to Ste2p (GPCR) at the Gpa1 (Gα) binding interface and obstruct the downstream signaling. Our computational results further suggest that hydrophobic ligands such as sterols strengthen the Ste2p-Gpa1p binding and might trigger a cohesive response that potentially obstructs downstream signaling. Experimental evidence further supported these findings that the elevated intracellular levels of these metabolites rescue the pheromone-induced PCD. To evaluate the evolutionary conservation and possible clinically relevant translation of this mechanism, we tested these metabolites on

human and rat isoproterenol-induced, GPCR-mediated cardiac hypertrophy model systems and observed attenuated response in the cardiomyocytes pretreated with GPCR-Gα-protein interface modulating metabolites.

RESULTS

Development and validation of Gcoupler

Designing novel target molecules by integrating the topological, chemical, and physical attributes of protein cavities necessitates advanced neural networks. While existing approaches like Bicyclic Generative Adversarial Networks (BicycleGANs) (30) and Recurrent Neural Network (RNNs) (31) have demonstrated potential, end-to-end standalone tools for GPCR-specific ligand design remain scarce. To address this, we developed Gcoupler, a Python package and Docker image for structure-based, cavity-dependent *de novo* ligand design, employing advanced Graph Neural Networks (GNNs) and robust statistical methods. Gcoupler consists of four interconnected modules, i.e., Synthesizer, Authenticator, Generator, and BioRanker, all together offering an intuitive workflow for ligand design, screening, and prioritization.

The Synthesizer module identifies putative cavities in protein structures, providing users with flexibility to select cavities based on druggability scores or user-supplied critical residues. Leveraging LigBuilder V3 (32), it generates cavity-specific ligands influenced by topology and pharmacophores, outputting SMILES, cavity coordinates, and other requisite files to downstream modules for further steps **(Figure 1a)**. By default, it synthesizes 500 molecules using a hybrid Growing-Linking mode optimized through genetic algorithms though it can also be user-defined. Notably, the fragment library of LigBuilder, comprising of 177 distinct molecular fragments in Mol2 format, allows the selection of multiple seed structures and extensions that best complement the cavity pharmacophores throughout multiple iterative runs. The Synthesizer module of Gcoupler enhances LigBuilder V3 for GPCR ligand design but lacks user-defined library screening, and proposes synthetically challenging molecules, and often requires post-processing to isolate high-affinity binders from a broad affinity range of synthetically designed compounds.

To address these challenges, we developed Authenticator which validates Synthesizer outputs by segregating high-and low-affinity binders (HABs and LABs) *via* virtual screening using the AutoDock Vina (33) and statistically testing the differences in the binding energies distributions using the Kolmogorov–Smirnov, Epps-Singleton, and Anderson-Darling Test. This module refines synthetic ligand pools by analyzing binding energy distributions, facilitating informed segregation while allowing user-defined thresholds and hypothesis testing for flexibility. The Generator, the third module, employs state-of-the-art GNN models such as Graph Convolution Model (GCM), Graph Convolution Network (GCN), Attentive FP

(AFP), and Graph Attention Network (GAT) to construct predictive classifiers using Authenticator-informed classes. With automated hyperparameter tuning and k-fold cross-validation, it ensures robust model training and minimizes overfitting. Notably, by default, Gcoupler employs three-fold cross-validation, but users can adjust this parameter.

Finally, BioRanker, the last module prioritizes ligands through statistical and bioactivity-based tools. The first level ranking offered by BioRanker is composed of a statistical tool that encompasses two distinct algorithms, namely G-means and Youden's J statistics, to assist users in identifying the optimal probability threshold, thereby refining the selection of high-confidence hit compounds (**Supplementary Figure 1a**). Additionally, bioactivity embeddings computed via Signaturizer (34) enable multi-activity-based ranking using a modified PageRank algorithm. Taken together, Gcoupler is a versatile platform supporting user-defined inputs, third-party tools for cavity selection, and customizable statistical analyses, enhancing its adaptability for diverse ligand design and screening tasks. This integrated framework streamlines cavity-specific ligand design, screening, and ranking, providing a comprehensive solution for GPCR-targeted drug discovery.

To evaluate Gcoupler's performance, we tested its modules across five GPCRs (AA2AR, ADRB1, ADRB2, CXCR4, and DRD3) using experimentally validated ligands and matched decoys from the DUD-E dataset (35). Gcoupler accurately identified orthosteric ligand-binding sites and additional allosteric cavities across all targets, validating its *de novo* cavity detection algorithm **(Supplementary Figure 1b)**. For orthosteric sites, the Synthesizer module generated ~500 compounds per GPCR, and the Authenticator module classified these into high- and low-affinity binders using thresholds optimized for each GPCR (-7 kcal/mol for AA2AR, CXCR4, DRD3; -8 kcal/mol for ADRB1, ADRB2) **(Supplementary Figure 1c)**. Statistical validation confirmed significant separation between these groups ($p < 0.0001$), enabling the Generator module to construct graph-based classification models with high values of AUC-ROC (>0.95), sensitivity, and specificity **(Figure 1b-c, Supplementary Figure d-e)**. These models reliably distinguished ligands from decoys, demonstrating Gcoupler's accuracy in identifying high-affinity ligands. We extended this validation to allosteric sites using three GPCR-ligand complexes (β2AR-Cmpd-15PA, CCR2-CCR2-RA-[R], CCR9-Vercirnon) from the PDB (36). Gcoupler successfully identified allosteric binding sites and generated classification models for synthetic compounds with consistently high AUC-ROC values (>0.95) **(Figure 1d, Supplementary Figure 2a-c)**. Projection of experimentally validated ligands onto these models further confirmed their predictive accuracy **(Figure 1e)**, underscoring Gcoupler's robustness and versatility for orthosteric and allosteric ligand discovery. We next benchmarked Gcoupler's efficiency against AutoDock

using the alpha-1A adrenergic receptor (993 agonists from ChEMBL31). Gcoupler was 13.5 times faster, leveraging its deep learning-based Generator module and AutoDock Vina's efficiency. Both methods provided comparable predictions for active compounds, demonstrating Gcoupler's speed and accuracy, making it ideal for large-scale ligand design and drug discovery **(Supplementary Figure 3a-h)**.

Finally we used Gcoupler to evaluate the ligand space conservation (functional conservation) of the GPCR-Gα interface. We analyzed multiple human GPCR-Gα complexes from the PDB **(Figure 1f, Supplementary Table 1)**, identifyed conserved motifs (DRY, CWxL, NPxxY) and binding pockets through sequence and structural analyses **(Figure 1g)**. Structural conservation was quantified by normalized RMSD values (mean: 1.47 Å; median: 0.86 Å), confirmed robust topological similarity at the GPCR-Gα interfaces **(Figure 1h-j, Supplementary Figure 3i-k, Supplementary Table 2)**. Using Gcoupler, ~50 ligands per GPCR were synthesized, with physicochemical property analysis (via Mordred) and revealed high cosine similarity, which further supports the functional conservation of GPCR-Gα interface **(Figure 1h, k, Supplementary Figure 3l, Supplementary Table 3)**. In summary, we used Gcoupler to systematically evaluate and analyze the ligand profiles of the GPCR-Gα-protein interface and observed a higher degree of sequence, topological, and functional conservation**.**

Gcoupler reveals endogenous, intracellular Ste2p allosteric modulators.

We next utilized Gcoupler to test the hypothesis that the intracellular metabolites could potentially and directly regulate the GPCR signaling by directly interacting with the GPCR-Gα-protein interaction interface **(Figure 1l)**. To test this hypothesis, we utilized a well-characterized yeast mating pathway mediated via the Ste2p-Gpa1p interface **(Supplementary Figure 4a)**. Gcoupler was employed to screen metabolites from the Yeast Metabolome Database (YMDB) against the yeast phospholipid bilayer-embedded molecular dynamics simulated cryo-EM structure of Ste2p **(Supplementary Figure 4b-i)**. This led to the identification of 17 potential surface cavities on Ste2p, with two intracellular regions, IC4 and IC5, accounting for over 95% of the Ste2p-Gpa1p interface **(Figure 2a-b, Supplementary Figure 4j-n)**. Conservation analysis of these cavities across 14 yeast species further confirmed their structural significance **(Supplementary Figure 4o)**. We independently ran Gcoupler for IC4 and IC5, compared their chemical diversity to ligands for the extracellular cavity (EC1), revealing distinct pharmacophore properties, and confirmed cavity-specific chemical spaces through principal component analysis (PCA) **(Supplementary Figure 5a-e)**. We further assessed the reproducibility of the Gcoupler by

synthesizing 100 in silico compounds per run across five runs for the Ste2p IC4 cavity. Analysis of chemical diversity via 2D/3D PCA and pairwise Tanimoto Similarity (atom-pair fingerprints) revealed heterogeneous yet overlapping chemical compositions among ligands across runs **(Supplementary Figure 5f-h)**.

Post these performance/reproducibility checks of Gcoupler, we finally generated high-affinity (HABs) and low-affinity (LABs) binders, screened yeast metabolites using a hyperparameter-tuned Graph Neural Network (Attentive FP), and predicted potential binders to IC4 and IC5 with a >0.5 binding probability. AutoDock-based molecular docking of YMDB metabolites against the cavities further refined our list, revealing metabolites with consensus binding energies ≤ -7 kcal/mol and binding probabilities >0.5 **(Figure 2c-f, Supplementary Figure 6a-f, Supplementary Table 4)**. Furthermore, HAMs (High-Affinity Metabolites) and LAMs (Low-Affinity Metabolites) displayed distinct atomic fingerprints, with enriched functional groups, including R2NH, R3N, ROPO3, ROH, and ROR, observed in HAMs **(Supplementary Figure 6g-h)**. Pathway enrichment analysis identified metabolites involved in steroid, sesquiterpenoid, and triterpenoid biosynthesis, along with folate pathways **(Figure 2g)**. BioRanker module further pinpointed sterols, including zymosterol (ZST), ubiquinone 6 (CoQ6), and lanosterol (LST), as top candidates, exhibiting high prediction probabilities (>0.99) and structural similarity to HABs **(Figure 2h, Supplementary Figure 6i-j)**. To validate Gcoupler-identified allosteric modulators, we performed control analyses of the Authenticator and Generator modules and blind docking of YMDB metabolites with Ste2p. Removing HAB and LAB labels from IC4 cavity compounds and applying random data splitting yielded poor model performance compared to Authenticator-guided splitting, confirming its robustness **(Supplementary Figure 6k)**. Increasing training data size (25%, 50%, 75%, 100%) improved model accuracy for YMDB metabolite projections **(Supplementary Figure 6l-m)**. Blind docking using AutoDock failed to distinguish HAM and LAM, unlike cavity-specific analysis via AutoDock and Gcoupler, which showed clear segregation (binding energy cutoff: -7 kcal/mol, Gcoupler probability: 0.5; **Supplementary Figure 6n**). All these rigorous control analyses and blind docking validated the reliability of Gcoupler's predictions, confirming its robustness in identifying cavity-specific modulators.

To experimentally validate the role of Gcoupler-predicted metabolites in Ste2p signaling, we performed a genetic screen of metabolic mutants. Mapping the predicted metabolites to KEGG and MetaCyc pathways revealed key enzymes involved in their metabolism.

Screening 53 single metabolic deletion mutants showed that most deletion mutants resisted α-factor-induced PCD, with some displaying accelerated growth, suggesting a metabolic modulation of Ste2 signaling **(Figure 2i-k, Supplementary Figure 7a-c, Supplementary Table 5)**. Notably, the *STE2* knockout mutant (*ste2Δ*) displayed no significant PCD induction, validating the importance of Ste2p in this process. To further investigate the metabolic pathways associated with PCD resistance, we conducted high-resolution metabolomics on yeast cells exposed to varying α-factor concentrations. Survivors of PCD induction exhibited differential metabolite profiles, with CoQ6 and ZST showing consistent enrichment across conditions **(Figure 2l-n, Supplementary Figure 7d-j, Supplementary Table 6)**. Pathway analysis of these metabolites indicated involvement in glyoxylate, dicarboxylate, purine, and vitamin B6 metabolism **(Supplementary Figure 7k)**. These findings, in conjunction with the genetic screen, highlight the interplay between metabolism and Ste2 signaling, with computationally predicted metabolites like ZST and CoQ6 potentially conferring resistance to α-factor-induced PCD.

Elevated Endogenous Metabolic levels selectively inhibit GPCR signaling.

To evaluate the stability of the interactions of zymosterol (ZST), lanosterol (LST), and ubiquinone 6 (CoQ6) at the Ste2p-Gpa1p interface, we performed molecular dynamics (MD) simulations (100 ns) for Ste2p-metabolite complexes. Results revealed thermodynamically stable interactions across cavities IC4 and IC5, except for CoQ6, which exhibited fluctuating RMSD in IC5 **(Figure 3a-c, Supplementary Figure 8a-b)**. Extended 550 ns simulations confirmed stability for ZST and LST in IC4, while CoQ6 showed RMSD fluctuations post 100 ns **(Supplementary Figure 8c)**. To gain further insight into the contributing residues from the MD simulations, we performed a residue-wise decomposition analysis that provides information about the energy contributions from the different residues to total binding free energies **(Supplementary Figure 9a)**. These results suggest that IC4 and IC5 specific residues predominantly contribute to the total binding free energies. Notably, the binding free energies are obtained as an average of over 500 configurations corresponding to the last 50 ns of the MD simulations.

To gain deeper insight into the mode of action of these metabolites in inhibiting Ste2p signaling, we first analyzed their impact at the orthosteric site, i.e., α-factor binding. We performed protein-peptide docking of Ste2p and α-factor and observed that metabolite-binding at the Ste2p-Gpa1p interface favors the α-factor interaction, as inferred from the binding free energies ΔG (kcal/mol) **(Supplementary Figure 9b-c)**. We also analyzed protein-protein interaction between the Ste2p (GPCR) and miniGpa1p (55) by selecting

GPCR configurations with and without metabolite-induced altered cavity topologies (IC4 and IC5), respectively (frames output from the aforementioned Ste2p-metabolite complex simulations) and computed the dissociation constant (Kd), binding affinity (ΔG) and the structural changes in the overall Ste2p topology **(Figure 3d-e, Supplementary Figure 9b-d)**. These computational analyses revealed that in contrast to metabolite-free Ste2p-Gpa1p interaction, referred to as wild-type (WT) condition, the Kd value is multi-fold lower in the presence of metabolite, indicating a cohesive response induced by these metabolites. A multi-fold lower Kd value further indicates and potentially explains that the metabolites binding favors Ste2p (GPCR) and miniGpa1-protein interaction and enables the establishment of a stable complex that might influence the shielding of the effector-regulating domains of the Gpa1p or influence its binding with the Ste4p (Gβ)-Ste18p (Gγ) complex.

We next asked whether the observed resistance toward α-factor-induced PCD in single metabolic mutants might be the direct consequence of the identified metabolites or a pleiotropic response due to an altered genome. To test this, we next exogenously elevated ZST, CoQ6, and LST levels (prediction probability > 0.99 and post-filtration using BioRanker) in wild-type yeast and observed selective modulation of Ste2p signaling. Pre-loaded cells exhibited rescue from α-factor-induced PCD across growth kinetics, PI-based viability, and FUN^{TM}1 assays while maintaining α-factor specificity over acetic acid-induced PCD **(Figure 3f-g, Supplementary Figure 10a-c)**. Mating assays further supported reduced Ste2p signaling in metabolite-preloaded cells, with CoQ6 showing no significant effects, consistent with its instability observed in molecular dynamics simulations **(Figure 3h, Supplementary Figure 10d)**. Further, we evaluated the deactivation of the pathway at the MAPK signaling level, where the α-factor-induced p-Fus3 levels were suppressed by ZST and LST **(Figure 3i)** but not CoQ6 (data not shown). Moreover, by using the P_{FUS1}-eGFP-CYC1 strain-based reporter assays, metabolite pre-treatment confirmed the inhibition of α-factor signaling **(Figure 3j)**. These findings suggest endogenous metabolites as modulators of Ste2p signaling by stabilizing Ste2p-Gpa1p interactions.

Site-Directed *Ste2* Mutants Abrogate Metabolite-Mediated Rescue Phenotype

To gain a deeper understanding, we investigated the role of metabolite binding in modulating Ste2p-Gpa1p interaction dynamics and employed both computational and experimental approaches. *In silico* site-directed mutagenesis of Ste2p revealed key metabolite-binding residues: S75 and R233 for CoQ6, L289 for ZST, and T155, V152, and I153 for LST. Prioritizing strong hydrogen bonds within an ideal 2.7–3.3 Å range, we selected mutants S75A, L289K, and T155D. These mutations significantly increased the dissociation constant

(Kd) of the Ste2p-Gpa1p complex, indicating weakened interactions compared to wild-type Ste2p **(Figure 4a-b, Supplementary Figure 11a)**. This computational evidence supports the hypothesis that metabolite binding stabilizes the Ste2p-Gpa1p complex, facilitating the rescue response to α-factor-induced programmed cell death (PCD).

Next, we performed experimental validation by generating site-directed mutants and confirmed these computational predictions. Mutants (S75A, L289K, T155D) expressed in a *ste2Δ* background **(Supplementary Figure 11b)** exhibited no rescue from α-factor-induced PCD upon pre-treatment with their respective metabolites, as shown by fluorometry-based cell death assays, FUN^{TM}1 staining, and p-Fus3 signaling analysis by mapping MAPK pathway activation **(Figure 4c-e)**. The lack of rescue highlights the direct role of metabolite binding at the Ste2p-Gpa1p interface in regulating downstream signaling. Interestingly, S75A mutants showed no α-factor-induced effects, likely due to significant structural disruptions. Shmoo formation assays further corroborated these findings, with no rescue effects observed in the mutants despite metabolite pre-loading **(Supplementary Figure 11c-e)**.

To gain mechanistic insights, we performed RNA sequencing on LST-preloaded and untreated (control) cells with and without α-factor exposure. Transcriptomic analysis revealed differential expression of genes implicated in PCD and mating responses, including *GSY1*, whose downregulation was linked to α-factor resistance **(Figure 4f-g, Supplementary Figure 12a-c, Supplementary Tables 7-10)**. Loss-of-function studies using knockout strains validated the involvement of key transcripts in metabolite-mediated rescue, particularly *YCR095W-A*, which exhibited a pronounced phenotype loss **(Supplementary Figure 12d-f)**. These results collectively suggest that metabolite binding at the Ste2p-Gpa1p interface directly drives rescue responses, with secondary contributions from differentially expressed genes in attenuating α-factor-induced cell death.

Finally, we explored whether intracellular allosteric modulators such as ubiquinone 6 (CoQ6), zymosterol (ZST), lanosterol (LST), fucosterol (FST), and ubiquinone 10 (CoQ10) modulate GPCR signaling in higher vertebrates such as human and rat beta 1/2-adrenergic receptors signaling. Notably, computational docking at the GPCR-Gα interface revealed strong binding affinities for these metabolites, similar to Ste2p-metabolite interactions **(Supplementary Figure 13a-b)**. Sequence conservation analysis of the GPCR-Gα interface across yeast Ste2p and adrenergic receptors in humans and rats further confirmed a high degree of evolutionary conservation at the metabolite-binding residues **(Supplementary Figure 13c)**. Finally, to test this functional relevance, we evaluated the effect of these metabolites on isoproterenol-induced adrenergic receptor-mediated cardiac hypertrophy in

human AC16 cardiomyocytes and neonatal rat cardiomyocytes. Preloading cells with these metabolites significantly attenuated hypertrophic responses, as evidenced by reduced single-cell surface area in quantitative assessments **(Figure 4h-j)**. Notably, to further evaluate the evolutionary conservation of this phenomenon, we also analyzed 75 unique GPCR-Gα complex structures from six species, selected from the PDB database. Dynamic docking was performed using five metabolites (CoQ6, ZST, LST, FST, and CoQ10) identified by Gcoupler as potential allosteric modulators and five negative controls predicted as poor binders. Results revealed significantly lower docking scores (<-7 kcal/mol) for Gcoupler-recommended metabolites compared to negative controls, irrespective of GPCR type or species **(Supplementary Figure 13d-h)**. These findings demonstrate that intracellular metabolite modulation of GPCR activity is a conserved mechanism extending beyond yeast to higher vertebrates.

DISCUSSION

Over the last few decades, extensive research has focused on identifying allosteric modulators of GPCRs due to their relevance in drug discovery (7, 20). Most known modulators are exogenous and target extracellular sites, while intracellular allosteric sites, identified recently through structural biology, offer novel avenues for regulation (3, 4, 6–8, 20). These sites, overlapping with G-protein and β-arrestin coupling regions, highlight the potential for intracellular allosteric modulation (1, 5, 8). Intracellular modulators, including chemically diverse agents like auto-antibodies and sodium ions, remain poorly understood, emphasizing the need for systematic exploration of these sites (4–6, 8, 9, 11–13, 37). However, the lack of data on intracellular modulators limits the feasibility of conventional computational approaches (14, 19, 38)(39–42).

To address this gap, we developed Gcoupler, a computational framework integrating *de novo* cavity identification, ligand synthesis, statistical analysis, graph neural networks, and Bioactivity-based ligand prioritization. Unlike existing tools, Gcoupler does not require cavity-specific experimentally validated compounds for model training. Gcoupler's precision in cavity mapping, flexibility for user-defined queries, and ability to screen large chemical libraries make it a versatile and efficient tool. Additionally, Gcoupler's generic design allows application beyond GPCRs, contrasting with existing platforms that often have limitations in modularity, precision, or open-source availability. Noteworthy, in contrast to other known allosteric sites identification tools for GPCRs, such as Allosite (43), AllositePro (44), AlloReverse (45), that largely leverage the ML-based models or require orthosteric ligand-bound structure as input, the cavity detection feature of Gcoupler (LigBuilderV3), a critical step for the entire workflow, is not limited to only the allosteric sites; instead, it identifies all possible cavity-like regions on the protein surface, which then gets classified into druggable, undruggable, or amphibious based on their individual scoring and ligandability, thus making it unbiased and more specific towards query protein. Notably, the rationale for opting for LigBuilder V3 for cavity identification over similar tools such as Fpocket (46) is that the former uses a hydrogen atom probe, moving along the protein surface grid of 0.5 Å for cavity detection, being much more precise in detecting cavity boundaries, in both breadth and depth mapping; in contrast, the latter considers clusters of alpha spheres **(Supplementary Table 11)**.

To date, only a few methods leverage generative AI models for cavity/pocket-based drug design. Gcoupler is an open-source, end-to-end platform integrating Ligand-Based Drug Design (LBDD) and Structure-Based Drug Design (SBDD) for drug design and large-scale

screening. Unlike Pocket Crafter (47), which requires proprietary tools (e.g., MOE QuickPrep) and lacks predictive model-building modules, Gcoupler offers comprehensive functionality. Similarly, DeepLigBuilder (23) and Schrodinger's AutoDesigner are either closed source or limited in features compared to Gcoupler. Comparative analysis highlights Gcoupler's unique advantages in precision, flexibility, and functionality **(Supplementary Table 11)**.

Using Gcoupler, we investigated the molecular basis of innate resistance to α-factor-induced programmed cell death (PCD) in yeast. Unlike humans, yeast possess only two GPCR systems, making their pheromone-sensing pathway ideal for focused study. Previous research predominantly identified downstream regulatory mechanisms (29, 48, 49); however, our findings suggest an upstream, receptor-level regulation via endogenous intracellular metabolites. Computational and experimental evidence pinpointed specific metabolites binding to the Ste2p-miniGpa1 interface, modulating signaling. Site-directed mutagenesis confirmed the functional relevance of these metabolite-interacting residues. Of note, previous mutagenesis experiments also revealed multiple critical amino acid residues that overlap with IC4 and IC5, suggesting their functional relevance in Ste2p downstream signaling **(Supplementary Table 12)**. Despite these advances, certain limitations remain, including the potential pleiotropic effects in metabolic gene knockouts and challenges in replicating natural metabolite concentrations. Mechanistic insights into sterol biosynthesis mutants (*ergΔ*) revealed impaired mating responses due to heterogeneous defects, such as reduced sterol accumulation and shmoo formation, impaired membrane fusion, and decreased *FUS1* expression (50–54). This highlights a novel role for sterols in GPCR regulation and their broader implications for yeast microbial factories and stress tolerance (55, 56). Sterols and other endogenous metabolites were shown to modulate GPCR activity by targeting conserved Gα-binding sites, reinforcing the evolutionary conservation of this mechanism across species, as demonstrated in human and rat hypertrophy models in this study.

In summary, our work uncovers a novel regulatory mechanism for GPCRs mediated by intracellular metabolites and presents a computational framework, Gcoupler, to explore unexplored allosteric sites. The proposed model suggests that selective metabolites binding to GPCR-Gα interfaces induce local conformational changes, stabilizing GPCR-G-protein complexes and potentially obstructing downstream signaling. Alternative mechanisms, such as orthosteric site modulation, kinase/arrestin interaction interference, or alterations in membrane dynamics, remain to be explored, warranting further investigation. A critical limitation of our study is the absence of direct binding assays to validate the interaction

between the metabolites and Ste2p. While our results from genetic interventions, molecular dynamics simulations, and docking studies strongly suggest that the metabolites interact with the Ste2p-Gpa1 interface, these findings remain indirect. Direct binding confirmation through techniques such as surface plasmon resonance, isothermal titration calorimetry, or co-crystallization would provide definitive evidence of this interaction. Another critical limitation of our findings is its reliance on tools like AutoDock and PRODIGY for preliminary binding affinity estimates, which lack the thermodynamic precision of advanced methods. To address this, we employed MD simulations with MM/GBSA, incorporating factors like protein flexibility and solvation effects for more accurate ΔG calculations. While computationally intensive approaches were beyond this study's scope, we ensured reported ΔG values reflected system conformational flexibility by basing them on pre-simulated docked structures from molecular dynamics simulations. Further, our results suggest that the metabolite binds to the Ste2p-Gpa1 interface and modulates receptor activity upon pheromone stimulation, as supported by various assays. However, the precise sequence of interactions between Ste2p, the metabolite, and Gpa1 remains unexplored, as it requires sequential experiments beyond this study's scope. Taken together, addressing these limitations in future work would significantly strengthen our conclusions and provide deeper insights into the precise molecular mechanisms underlying the observed phenotypic effects.

MATERIAL AND METHODS

Backend code for the Gcoupler

The back-end code for Gcoupler is implemented entirely in Python (3.8) and comprises four modules: Synthesizer, Authenticator, Generator, and BioRanker. Synthesizer employs LigBuilder V3.0 (32) for *de novo in silico* ligand synthesis, identifying protein cavities likely to be active or allosteric sites using a hybrid GROW-LINK approach with a Genetic Algorithm. The module autonomously selects one cavity for ligand synthesis based on user-defined residue positions. Using the CAVITY function of LigBuilder (27), it classifies 3D grid points around the protein into occupied, vacant, and surface points and integrates geometric and physicochemical properties to identify binding sites (57). Synthesizer outputs ligand structures in SMILES and PDBQT formats, alongside cavity grid coordinates for downstream modules. Authenticator validates the synthesized ligands using AutoDock Vina (1.2.3) for virtual screening (33). Binding energy calculations classify ligands into High-Affinity Binders (HABs) and Low-Affinity Binders (LABs), preserving balance for subsequent deep learning analysis. The default energy threshold is set to -7 kcal/mol, but users can explore alternative cutoffs, visualize distributions, and perform statistical comparisons within the workflow. These steps ensure precise identification and prioritization of ligand candidates for further analysis. The Authenticator uses the Kolmogorov-Smirnov test (58), Anderson-Darling test (59), and Epps-Singleton test (60) for hypothesis testing for the comparison of the distributions. The Authenticator module visualizes ligand distributions using overlapping density plots and Empirical Cumulative Distribution Function (ECDF) curves. If the default threshold fails to produce statistically meaningful separation, users can supply alternative negative datasets, such as decoys generated via Gcoupler's inbuilt RDKit Chem module or custom datasets (61). The Generator module builds deep learning-based classification models using the DeepChem (2.6.1) library (62). It accepts High-Affinity Binders (HABs) and Low-Affinity Binders (LABs)/decoys from the Authenticator module to train four graph-based models: Graph Convolution Model (GCM), Graph Convolution Network (GCN) (63), Attentive FP (AFP) (64), and Graph Attention Network (GAT) (65). Class imbalance is addressed through upsampling techniques. Generator tests all models using default hyperparameters, returning performance metrics for user selection. Hyperparameters can be tuned via manual settings or using default values followed by k-fold cross-validation. The final optimized model, trained on the complete synthetic dataset (HAB + LAB/decoys), enables large-scale screening of user-supplied compounds based on their SMILES representations. The BioRanker module performs post-prediction analysis for functional activity-based compound screening. Positively predicted compounds are selected using a stringent probability

threshold or adaptive methods such as G-means and Youden's J statistic, which optimize sensitivity and specificity. The selected compounds are projected into biological activity spaces (Chemistry, Targets, Networks, Cells, Clinics) by comparing their biological activity descriptor vectors with those of HABs using cosine similarity (34). A modified PageRank algorithm ranks compounds based on activity-specific scores, with support for multi-activity ranking to refine results based on user-defined biological properties, ensuring precise and context-relevant compound prioritization.

Additional information about the backend code for Gcoupler along with methodolody for Runtime analysis, Sequence-structural-functional level analysis, Molecular Dynamics Simulation, Molecular docking (AutoDock), Functional enrichment analysis, and Protein-protein docking can be accessed in the **Supplementary Information**.

Gcoupler Benchmarking

To assess batch effects across Gcoupler runs for a specific cavity, we utilized the standard Gcoupler Docker image. Intracellular cavity 4 (IC4) of the Ste2 protein of yeast was used for benchmarking. A total of 100 molecules were *in silico* synthesized by the Synthesizer module of Gcoupler iteratively. Post-generation, atom pair fingerprints (ChemmineR; R package) were calculated for the synthesized molecules from each run, and the data was visualized using Principal Component Analysis and pairwise comparison using Tanimoto Similarity (ChemmineR, R package).

For model benchmarking, Gcoupler was validated on GPCRs from the DUD-E dataset, alongside the information about the active ligands and their randomly selected number-matched decoys (35). Additionally, Gcoupler's performance in identifying experimentally elucidated allosteric sites and modulators was tested using PDB complexes obtained from the RCSB PDB database.

Metabolomics

Wildtype (BY4741) and *ste2Δ* yeast strains were grown in YPD medium at 30°C, 150 rpm, through primary and secondary cultures (16 hours each). Equal cell numbers (1.5 mL) were aliquoted into a 96-well deep well plate. α-factor (Sigma-Aldrich) was added at final concentrations of 10, 20, 30, 40, and 50 μM (eight replicates each). DMSO served as the solvent control, while untreated WT and *ste2Δ* conditions received no treatment. Plates were incubated (30°C, 150 rpm, 4 hours) under a breathable membrane. A 50 μL aliquot was taken for Propidium Iodide (PI; 11195, SRL) assay as described in **Supplementary**

Information. Following the PI assay, four pooled replicates were pelleted (6000 rpm, 5 min, RT), treated with zymolyase (40 U/mL, 1X PBS, 30°C, 1 hour), washed with PBS, and metabolomics analysis was performed. Data analysis included peak normalization, omission of metabolites with constant or >50% missing values, and kNN-based imputation (MetaboAnalyst). Data were IQR-filtered, and differentially enriched metabolites (DEMs) were identified by calculating log2 fold change ($|\log2FC| \geq 1$, $p < 0.05$ via Student's t-test). Pathway Over-Representation Analysis (ORA) was performed using MetaboAnalyst with hypergeometric or Fisher's exact tests to assess pathway enrichment against background metabolite distributions. Further details about methodology is available in **Supplementary Information**.

Genetic Screening

Fifty-three knockout strains from the Yeast Deletion Collection, along with WT and *ste2Δ*, were treated with α-factor (30 μM), while DMSO served as the solvent control. Plates were incubated for 4 hours. A 50 μL aliquot was used to measure Propidium iodide-based cell viability assessment assay as described in Supplementary Information. Fluorescence data were normalized to blank-adjusted OD600, followed by two additional rounds of normalization with unstained and HK controls. Percentage fold change for the treated group was calculated relative to the untreated group, and statistical significance was determined using a one-sample Student's t-test. Further details about the methodology used is available in **Supplementary Information**.

Pre-loading of Yeast cells with metabolite

Yeast cells were cultured in YPD medium at 30°C, 200 rpm for 16 hours in primary and secondary cultures. Equal cell densities (5 μL) from secondary cultures were inoculated into 96-well plates containing 145 μL YPD with metabolites Coenzyme Q6 (CoQ6, 900150O, Avanti® Polar Lipids), Zymosterol (ZST, 700068P, Avanti® Polar Lipids), and Lanosterol (LST, L5768, Sigma-Aldrich) at 0.1 μM, 1 μM, and 10 μM concentrations. Plates were incubated for 24 hours at 30°C, 200 rpm, with multiple biological replicates. Ethanol-treated wells served as solvent controls. For site-directed *STE2* mutants, the mutants were grown in

YPD for primary and secondary cultures, but the metabolite pre-loading was performed in YPGR instead of YPD to induce Ste2 expression.

After pre-loading, the following assays were performed: growth kinetics, propidium iodide-based assay, FUN^{TM}1 staining, Mating assay, Phospho-MAPK activity based-western blot and Transgenic reporter assay. The detailed protocol for each of these assays is available in **Supplementary Information**.

RNA-Sequencing

Yeast cells (BY4741) were cultured in YPD medium at 30 °C, 200 rpm, with or without lanosterol (LST, 1 µM) in biological duplicates. Cells were subsequently treated or untreated with α-factor (30 µM) for 2 hours. RNA was isolated following Mittal et al. (66). Sequencing quality was assessed using MultiFastQ, and paired-end reads were trimmed and aligned to the S. cerevisiae reference genome (ENSEMBL R64-1-1; GCA_000146045.2) using the Rsubread package (v2.6.4). Gene expression counts were generated via featureCounts and normalized using TMM **(Supplementary Table 7)**. Differential expression analysis was performed with NOISeq (v2.38.0) **(Supplementary Tables 8–10)**. Functional enrichment was assessed using the Gene Ontology Term Finder (v0.86) from the Saccharomyces Genome Database. Raw FASTQ files and normalized expression data are available on Zenodo. Additional details are available in the **Supplementary Information**.

Site-Directed Mutagenesis

The gene encoding wild-type *STE2* was PCR amplified from the genome of *Saccharomyces cerevisiae* and further cloned into plasmid pRS304 under galactose-inducible *GAL1* promoter to generate plasmid pRS304-P_{GAL1}-STE2-CYC1 using Gibson assembly (67, 68). The mutants were generated by PCR amplifying the gene with primers consisting of respective mutations and cloned into plasmid pRS304 under *GAL1* promoter to generate pRS304-P_{GAL1}-STE2 S75A-CYC1, pRS304-P_{GAL1}-STE2 T155D-CYC1, and pRS304-P_{GAL1}-STE2 L289K-CYC1. Wild-type (rtWT) and mutant *STE2* were integrated by digesting the pRS304 vector with restriction enzyme BstXI to generate linearized plasmid and transformed into *Saccharomyces cerevisiae* BY4741 *ste2Δ* strain. Additional details about the methodology is available in **Supplementary Information**

Cardiomyocytes Hypertrophy Models

Human AC16 cardiomyocytes were cultured in DMEM-F12 (Thermo Scientific) with 12.5% fetal bovine serum (FBS) at 37°C and 5% CO2. Cells were seeded in a 24-well plate for size

measurements, treated after 24 hours with metabolites (CoQ6, ZST, LST, FST, CoQ10) at 2.5 μM, and incubated overnight with 1% FBS. The medium was refreshed with fresh metabolites and isoproterenol (25 μM) for 48 hours. Cells were washed with PBS, fixed with 4% paraformaldehyde, and stained with wheat germ agglutinin (Thermo Scientific) and DAPI. Images were captured using a Leica DMI 6000 B microscope at 20X magnification, and cell area was measured using ImageJ. Neonatal rat cardiomyocytes were isolated from 1-3-day-old SD rat pups using Collagenase Type II. After heart explantation and digestion, the cells were centrifuged and pre-plated for 90 minutes to remove fibroblasts. The cardiomyocytes were seeded in a gelatin-coated 24-well plate, incubated overnight with 2.5 μM metabolites and 1% FBS, and then treated with metabolites (2.5 μM) and isoproterenol (10 μM) for 72 hours. Cells were fixed, stained with alpha-sarcomeric actinin and DAPI, and images were captured using a Leica DMI 6000 B at 20X magnification. Cell area was quantified using ImageJ. Additional details about methodology is available in **Supplementary Information**.

Statistical Analysis

Statistical analyses were performed using Past4 software or R-Programming. The Mann-Whitney U test was applied to compare medians between two distributions (non-parametric), while Student's t-test was used for pairwise comparisons of means. P-value correction was performed using the Bonferroni method when necessary. A significance threshold of 0.05 was set, with *, **, ***, and **** indicating p-values <0.05, <0.01, <0.001, and <0.0001, respectively.

Data Availability

The processed untargeted metabolomics data is provided as Supplementary Information. The raw RNA sequencing files are available at ArrayExpress under accession *E-MTAB-12992*.

Code Availability

A Python package for Gcoupler is provided via pip https://test.pypi.org/project/Gcoupler/. A docker container pre-compiled with Gcoupler and all of its dependencies can be found at https://hub.docker.com/r/sanjayk741/gcoupler. The source code of Gcoupler is available on the project GitHub page: https://github.com/the-ahuja-lab/Gcoupler and also at Zenodo with DOI: 10.5281/zenodo.7835335, whereas the raw sequencing files can be accessed using DOI: 10.5281/zenodo.7834294.

Ethical statement

The local IAEC (Institutional Animal Ethics Committee) committee at CSIR-Central Drug Research Institute approved all the animal experiments (IAEC/2020/38) following the guidelines of the Committee for the Purpose of Control and Supervision of Experiments on Animals (CPCSEA), New Delhi, Government of India.

Acknowledgments

The authors thank the IT-HelpDesk team of IIIT-Delhi for assisting with the computational resources. We thank all the members of the Ahuja lab for their intellectual contributions at various stages of this project. We thank Prof. G.P.S Raghava for providing critical comments on our manuscript. We thank Dr. Arjun Ray for providing intellectual support. We also thank Dr. Martin Graef and Dr. Kaushik Chakraborty for sharing yeast strains and the NIPER Guwahati central facility for helping us with high-resolution metabolomics. The Ahuja lab is supported by the Ramalingaswami Re-entry Fellowship (BT/HRD/35/02/2006), a re-entry scheme of the Department of Biotechnology, Ministry of Science & Technology, Government of India, Start-Up Research Grant (SRG/2020/000232) from the Science and Engineering Research Board, and a research grant from IHUB Anubhuti (Project Grant/23) and an intramural Start-up grant from Indraprastha Institute of Information Technology-Delhi. The INSPIRE faculty grant from the Department of Science & Technology, India, funds the Sengupta lab. Gupta Lab is funded by the Ramalingaswami Re-entry Fellowship (BT/RLF/re-entry/14/2019) from the Department of Biotechnology, Government of India.

FIGURE LEGENDS

Figure 1: Development, Benchmarking and Validation of Gcoupler Computational Framework.

(a) Schematic workflow depicting different modules of the Gcoupler package. Of note, Gcoupler possesses four major modules, i.e., Synthesizer, Authenticator, Generator and BioRanker. **(b)** AUC-ROC curves of the finally selected model for each of the indicated GPCRs. Note: Experimentally validated active ligands and decoys were used in the testing dataset. **(c)** Bar graphs depicting the sensitivities and specificities of the indicated GPCRs with experimentally validated active ligands and reported decoys. **(d)** The AUC-ROC curve indicating the model performance in the indicated conditions. **(e)** Bar graphs indicating the prediction probabilities for each indicated experimentally validated ligand. **(f)** Schematic workflow illustrates the steps in measuring and comparing the structural conservation of the GPCR-Gα-protein interfaces across human GPCRs. **(g)** Snakeplot depicting the standard human GPCR two-dimensional sequence level information. Conserved motifs of the GPCR-Gα-protein interfaces are depicted as WebLogo. Asterisks represent residues of conserved motifs present in the GPCRs-Gα-protein interfaces. Of note, the location of the motifs indicated in the exemplary GPCR snake plot is approximated. **(h)** Schematic workflow illustrates the steps in measuring and comparing the structural conservation of the GPCR-Gα-protein interfaces across human GPCRs. **(i)** Representative structures of the proteins depicting highly conserved (low RMSD) and highly divergent (high RMSD) GPCR-Gα-protein interfaces. PDB accession numbers are indicated at the bottom. **(j)** Heatmap depicting the RMSD values obtained by comparing all the GPCR-Gα-protein interfaces of the available human GPCRs from the protein databank. Of note, the RMSD of the Gα-protein cavity was normalized with the RMSDs of the respective whole proteins across all pairwise comparisons. **(k)** Heatmap depicting the pairwise cosine similarities between the *in silico* synthesized ligands of the GPCR-Gα-protein interfaces of the available human GPCRs using Gcoupler. **(l)** Schematic diagram depicting the hypothesis that the intracellular metabolites could allosterically modulate the GPCR-Gα interaction.

Figure 2: Identification of Endogenous, Intracellular Allosteric Modulators of Ste2p Using Gcoupler

(a) Schematic diagram depicting the topology of all the cavities identified using the Synthesizer module of the Gcoupler python package. Of note, the cavity nomenclature includes the cavity location, i.e., EC (extracellular), IC (intracellular), and TM (transmembrane), succeeded by numerical number. **(b)** Diagram depicting the three-dimensional view of the Ste2 protein, with highlighted Gα-protein binding site (Gpa1) and the

Gcoupler intracellular cavities (IC4 and IC5). The venn diagram at the bottom depicts the percentage overlap at the amino acid levels between the Gα-binding site and predicted IC4 and IC5. **(c)** Schematic representation of the overall workflow used to predict the endogenous intracellular allosteric modulators of Ste2 receptor using Gcoupler and molecular docking technique. Of note, Yeast Metabolome DataBase (YMDB) metabolites were used as query compounds. **(d)** Overlapping density plots depicting and comparing the distributions of synthetic compounds predicted to target the IC4 and IC5 of the Ste2 receptor using the Gcoupler package. Of note, the Authenticator module of Gcoupler segregated the synthesized compound for each cavity (IC4 or IC5) into High-Affinity Binders (HAB) and Low-Affinity Binders (LAB). **(e)** AUC (Area under the curve) plots representing the performance of the indicated models. Notably, the models were trained using the cavity-specific synthetic compounds generated using the Gcoupler package. **(f)** Scatter plots depicting the relationship (correlation) between the binding prediction probabilities using Gcoupler and binding free energies computed using molecular docking (AutoDock). **(g)** Scatterplot depicting the Pathway Over Representation Analysis (ORA) results of the endogenous metabolites that were predicted to bind to the GPCR-Gα-protein (Ste2p-Gpa1p) interface using both Gcoupler and molecular docking. **(h)** Alluvial plot showing five level sub-activity spaces screening of the selected metabolites for IC4. **(i)** Schematic diagram depicting the workflow opted to narrow down on the single metabolic gene mutants. **(j)** Schematic diagram depicting the experimental design used to screen single metabolic gene mutants for α-factor-induced PCD. Cell viability was assessed using Propidium iodide-based fluorometric assay. **(k)** Scatter plot depicting the impact of α-factor stimuli on cellular viability, assessed using Propidium iodide-based fluorometric assay. The y-axis represents -log10(p-value) of the one-sample student's t-test between the normalized PI fluorescence of untreated and treated conditions. The x-axis represents the percentage inhibition or increase in cellular viability, estimated using a Propidium Iodide-based assay. The mutants reported to be involved in mating, PCD, or both are indicated in orange, green, and blue, respectively. The statistically non-significant mutants are indicated below the dashed line in black. **(l)** Heatmap depicting the relative enrichment/de-enrichment of differentially enriched metabolites in the indicated conditions. Of note, four biological replicates per condition were used in the untargeted metabolomics. **(m)** Venn diagram depicting the overlap between the predicted endogenous intracellular allosteric modulators of Ste2p and differentially enriched metabolites (DEMs) identified using untargeted metabolomics. **(n)** Mean-whisker plot depicting the relative abundance of ubiquinone 6 (CoQ6) and zymosterol (ZST) in the indicated conditions. Student's t-test was used to compute statistical significance. Asterisks indicate statistical significance, whereas ns represents non-significance.

Figure 3: Elevated Endogenous Metabolite Levels Stabilize Ste2p-Gpa1p Interactions and Selectively Inhibit GPCR Signaling

(a) Scheme representing the key steps opted for preparing Ste2p structure for downstream computational analysis. **(b)** Barplots depicting the binding energies obtained by the docking of Ste2p and indicated metabolites across IC4 and IC5. **(c)** Line plots depicting the Root Mean Square Deviation (RMSD) changes over simulation timeframes from the three independent replicates of the indicated conditions in the indicated conditions. The spread of the data is indicated as Standard Deviation (SD). Notably, RMSD is provided in Angstroms (Å), whereas the simulation time is in nanoseconds (ns). **(d)** Workflow depicting the steps involved in Ste2p-miniG-protein docking using HADDOCK and PRODIGY web servers. **(e)** Barplots depicting the fold change of the dissociation constant (Kd) in the indicated conditions. Notably, fold change was computed with respect to the wild-type condition (Ste2p-miniG-protein). Inlets represent molecular representations of Ste2p-miniG-protein and the highlighted interface residues. **(f)** The schematic diagram depicting the experimental workflow used to quantify α-factor-induced PCD using a propidium iodide-based cell viability fluorometric assay. Box plot on the right depicting the rescue from the α-factor-induced PCD in the indicated conditions as inferred using propidium iodide-based cell viability fluorometric assay (n=9 or 10 biological replicates; Heatkilled = 2). The y-axis represents the fold change of the propidium iodide fluorescence values with respect to their respective controls. Mann Whitney U test was used to calculate statistical significance. Asterisks indicate statistical significance, whereas ns represents non-significance. **(g)** Schematic representation (left) of the experimental approach used to measure cell vitality and viability using microscopy-based FUN^{TM}1 staining. Representative micrographs (right) depicting the FUN^{TM}1 staining results in the indicated conditions, Scale 10 µm. Mean-whisker plot depicting the relative proportion of the vital and viable yeast cells observed using FUN^{TM}1 staining in the indicated conditions (n = 3 biological replicates). A Student's t-test was used to compute statistical significance. Asterisks indicate statistical significance, whereas ns represents non-significance. Error bars represent the standard error of the mean (SEM). **(h)** Schematic representation (left) of the experimental design for the mating assay (n = 3 biological replicates, each with three technical replicates). MATa yeast cells were preloaded with the metabolites and then mated with MATα cells to evaluate the mating efficiency. Representative micrographs in the middle qualitatively depict the mating efficiency in the indicated conditions. The bar plots on the right depict the mating efficiency (mean ± SEM) in the indicated conditions. Student's t-test was used to compute statistical significance. Asterisks indicate statistical significance, whereas ns represents non-significance. **(i)** Schematic representation depicting the experimental design of phospho-MAPK activity-based Western blot. Barplots depicting the p-Fus3 levels (mean ± SEM) in the indicated conditions. Error bars representing standard error of mean

(SEM). A Student's t-test was used to compute statistical significance. Asterisks indicate statistical significance, whereas ns represents non-significance. **(j)** Schematic representation (left) of the experimental approach used to measure the fluorescence in P_{FUS1}-eGFP-CYC1 yeast cells. Representative micrographs (right) depicting the eGFP expression in the yeast cells in the indicated conditions. Scale 20 µm. Barplot depicting the Corrected Total Cell Fluorescence (CTCF) value (mean ± SEM) in the indicated conditions. A Student's t-test was used to compute statistical significance. Asterisks indicate statistical significance, whereas ns represents non-significance.

Figure 4: Site-Directed Ste2p Mutants Disrupt Metabolite-Mediated Rescue

(a) Workflow depicting the steps involved in Ste2p-miniG-protein docking of the wild-type and site-directed Ste2p mutants. Notably, docking was performed using HADDOCK and PRODIGY web servers. **(b)** Barplots depicting the dissociation constant (K_d) fold change in Ste2p site-directed mutants and wild-type. Notably, fold change was computed with respect to the metabolite influenced wild-type condition (Ste2p-miniG-protein). **(c)** The schematic diagram depicting the experimental workflow used to quantify α-factor-induced programmed cell death in generated site-directed missense mutants (T155D, L289K, S75A), alongside reconstituted wild-type *STE2* (rtWT), using a propidium iodide-based cell viability fluorometric assay. The box plot (left) depicts the increase in the relative proportion of dead cells upon α-factor exposure. Box plot (right) depicting the loss of rescue phenotype from the α-factor-induced programmed cell death in the indicated conditions when pre-loaded with metabolites as inferred using propidium iodide-based cell viability fluorometric assay. The y-axis represents the fold change of the propidium iodide fluorescence values with respect to their respective controls. Mann Whitney U test was used to calculate statistical significance. Asterisks indicate statistical significance, whereas ns represents non-significance. **(d)** Schematic representation (top) of the experimental approach used to measure cell vitality and viability using microscopy-based FUN™1 staining. Representative micrographs (below) depicting the FUN™1 staining results in the indicated conditions, Scale 10 µm. Mean-whisker plot depicting the relative proportion of the vital and viable yeast cells observed using FUN™1 staining in the indicated conditions (n = 4 biological replicates). A Student's t-test was used to compute statistical significance. Asterisks indicate statistical significance, whereas ns represents non-significance. Error bars represent the standard error of the mean (SEM). **(e)** Schematic representation (up) depicting the experimental design of phospho-MAPK activity-based Western blot. Barplots (down) depicting the p-Fus3 levels (mean ± SEM) in the indicated conditions. The y-axis represents the p-Fus3/Fus3 ratio for the stimulated condition normalized by its corresponding unstimulated sample. A Student's t-test was used to compute statistical significance. Asterisks indicate statistical significance,

whereas ns represents non-significance. **(f)** Schematic representation depicting the experimental design of RNA sequencing, featuring treatment duration and the sequencing parameters. **(g)** Heatmap depicting the expression of differentially expressed genes obtained from RNA sequencing in the indicated conditions. Notably, Control and LST represent yeast cells unloaded and pre-loaded with lanosterol, respectively. α-factor is represented as α, where plus and minus signs represent its presence and absence, respectively. **(h)** Schematic representation of the experimental workflow followed to deduce the impact of indicated metabolites treatment on isoproterenol (ISO)-induced, GPCR-mediated hypertrophy response in human (AC16) and neonatal rat cardiomyocytes. Notably, in the case of AC16 cells, Wheat germ agglutinin (WGA) was used to stain the cardiomyocytes, whereas, for neonatal cardiomyocytes, alpha-sarcomeric actinin staining was used. **(i)** Micrographs depicting the human (above; green colored) and neonatal rat (below; red colored) cardiomyocytes in the indicated conditions. Scale 50 µm. **(j)** Box plots depicting the surface area of human (AC16) and neonatal rat cardiomyocytes in the indicated conditions. Statistical significance of indicated metabolites with untreated control and isoproterenol-treated conditions are indicated in green and grey text, respectively. Mann Whitney U test with Bonferroni corrected p-values was used to compute statistical significance.

SUPPLEMENTARY FIGURE LEGENDS

Supplementary Figure 1: Gcoupler Benchmarking using experimentally validated orthosteric ligands of GPCRs

(a) AUC-ROC curves depicting the optimal probability cutoff recommended by G-means and Youden J index algorithms, respectively. Notably, the optimal threshold is indicated by the black dot on the ROC curve. **(b)** Molecular representation depicting the indicated experimentally validated orthosteric sites of the AA2AR, ADRB1, ADRB2, CXCR4, and DRD3 receptors, with the zoom-in inlet on the right highlighting the ligand and the cavity topologies. **(c)** Overlapping density plots comparing the distributions of synthetic compounds predicted to target the indicated receptors into High-Affinity Binders (HAB) and Low-Affinity Binders (LAB) using the Authenticator module of Gcoupler package. **(d)** Bar graphs indicating the performance of the indicated models made for the experimentally elucidated orthosteric sites of the indicated GPCRs, generated using Gcoupler workflow. **(e)** Confusion matrices indicating the relative proportions of experimentally determined ligands and their respective decoys (randomly selected to match # of ligands for each receptor). Note the number of active ligands and decoys is mentioned at the bottom.

Supplementary Figure 2: Gcoupler Benchmarking using experimentally validated allosteric ligands of GPCRs

(a) Molecular representation of the β2AR, CCR2, and CCR9 receptors with highlighted experimentally validated intracellular allosteric cavity and ligand. **(b)** Overlapping density plots comparing the distributions of synthetic High-Affinity Binders (HAB) and Low-Affinity Binders (LAB) predicted to target the allosteric cavities of the indicated GPCRs using the Gcoupler package. **(c)** Bar graphs depicting the performance metrics of the indicated classification model generated using Gcoupler for the highlighted allosteric cavities of the indicated proteins.

Supplementary Figure 3: Run Time comparison of Gcoupler and AutoDock

(a) Flowchart depicting the entire workflow used to compute and compare the runtime using AutoDock and Gcoupler. Of note, the Synthesizer, Authenticator, and Generator module of Gcoupler are indicated alongside their key processes. **(b)** Ribbon diagram depicting the ADRA1A predicted structure using Alphafold (ID: AF-P35348). **(c)** A waterfall chart depicts the timestamp information about the key steps involved in AutoDock. Time consumed at the indicated steps is mentioned in seconds and hours along the y-axis and above bars, respectively. **(d)** Waterfall chart depicting the timestamp information about the key steps involved in Gcoupler. Time consumed at the indicated steps is mentioned in seconds and

hours along the y-axis and above bars, respectively. **(e)** Bar plot depicting the comparison between the total time consumed by the AutoDock and Gcoupler to predict the binding of experimentally validated ligands for ADRA1A (AF-P35348). **(f)** Boxplot depicting the performance metrics of the 10-fold cross-validation of the training data obtained using Gcoupler. **(g)** Boxplot depicting the performance metrics of the 10-fold cross-validation of the testing data obtained using Gcoupler. **(h)** Scatterplot depicting the relationship between AutoDock computed binding energies and Gcoupler computed prediction probabilities of the experimentally validated ligands of ADRA1A protein. **(i)** Density plot depicting the distribution of RMSD between GPCR-Gα cavity across selected GPCRs-G-protein pairs. Of note, the RMSD of the Gα-protein cavity was normalized with the RMSDs of the respective whole proteins across all pairwise comparisons. **(j)** Heatmap depicting the RMSD values obtained by comparing all the GPCR-Gα-protein interfaces of the available human GPCRs from the protein data bank. **(k)** Heatmap depicting the RMSD values obtained by comparing the selected human GPCRs available in the protein data bank. **(l)** Density plot depicting the distribution cosine similarities among the *in silico* synthesized ligands of the GPCR-Gα-protein interfaces of the available human GPCRs using Gcoupler.

Supplementary Figure 4: Ste2 protein cavities prediction using Gcoupler

(a) Schematic diagram depicting the hypothesis that the intracellular yeast metabolites could allosterically modulate the GPCR-Gα-protein (Ste2p-Gpa1p) interface and, therefore, the Ste2p signaling pathway in yeast. **(b)** Overlapping Ste2p (GPCR) ribbon diagram depicting the structural similarity between the experimentally elucidated Ste2p structure before and after molecular dynamics simulation using GROMACS software. RMSD value is depicted at the bottom. **(c)** Flowchart depicting the key steps used for the molecular dynamics simulation of the Ste2p using CHARMM-GUI and GROMACS software. **(d)** Line plot depicting the changes in the density (kg/m^3) along the z-axis of the three-dimensional Ste2p structure. **(e)** Line plot depicting the decline in the potential (kJ/mol) over molecular dynamics simulation time in picoseconds (ps). **(f)** Line plot depicting the changes in the density (kg/m^3) of the overall system over molecular dynamics simulation time in picoseconds (ps). **(g)** Line plots depicting the changes in the pressure (in bars) and temperature (in Kelvin) of the overall system during molecular dynamics simulation of Ste2 protein. **(h)** Line plot depicting the Root Mean Square Deviation (RMSD) changes of the Ste2 protein during molecular dynamics simulation. Note the RMSD values are indicated in nanometers (nm). **(i)** Ramachandran plot depicting the location of simulated Ste2 protein residues in the favorable and unfavorable regions. **(j)** Barplot depicting the predicted cavities volumes (Å). **(k)** Scatterplot depicting the relationship between the cavity volume and surface area in the indicated cavities of the Ste2 protein. **(l)** Heatmap depicting the percentage of amino acids of

the indicated cavities residing in the EC (extracellular), IC (intracellular), and TM (transmembrane) region of the Ste2 protein. **(m)** Scatterplot depicting the predicted drug score of the indicated cavities of the Ste2 protein. **(n)** Snake plot depicting the key amino acids of the Ste2 protein alongside their location within the indicated functional cavities. **(o)** Snake plot depicting the conservation of Ste2 protein at the amino acid levels. Of note, Ste2 proteins from 15 related yeast species were used for computing the conservation score.

Supplementary Figure 5: Comparison of chemical composition of cavity-specific ligands of Ste2 protein.

(a) Venn diagram depicting the number of overlapping amino acids constituting the Extracellular Cavity 1 (EC1), Intracellular Cavity 4 (IC4), and Intracellular Cavity 5 (IC5) of the Ste2p. **(b)** Two-dimensional and **(c)** three-dimensional Principal Component Analysis plots depicting the segregation of *in silico* synthesized ligands for the indicated cavities via Gcoupler. Of note, atom pair fingerprints were used as features for this analysis. **(d)** Scatter plot depicting the relationship between the depth of the pharmacophore features and the neighboring grids. **(e)** Donut charts illustrating the properties of amino acids constituting the pharmacophore for each of the indicated cavities. **(f)** Two-dimensional and **(g)** three-dimensional Principal Component Analysis plots depicting the chemical properties of *in silico* synthesized ligands from five independent runs on the IC4 of the Ste2p using the Gcoupler Synthesizer module. Of note, atom pair fingerprints were used as features for this analysis. **(h)** Heatmap depicting the Tanimoto Similarities scores between the synthesized ligands for IC4 of Ste2p across five independent runs using Gcoupler.

Supplementary Figure 6: Sanity Check of Gcoupler Predictions.

(a) Principal Component Analysis depicting chemical heterogeneity of synthetic compounds synthesized using Gcoupler across intracellular cavities (IC4 and IC5). Notably, the compounds were segregated into High-Affinity Binders (HAB) and Low-Affinity Binders (LAB) by the Authenticator module of the Gcoupler. **(b)** Heatmap depicting the chemical similarity of the *de novo* synthesized HAB (dark green) and LAB (light green) across intracellular cavities (IC4 and IC5) of the Ste2 protein. Tanimoto similarities were computed using Atomic fingerprints. **(c)** Heatmaps illustrating the relative enrichment of the indicated functional groups (RNH2: primary amine, R2NH: secondary amine, R3N: tertiary amine, ROPO3: monophosphate, ROH: alcohol, RCHO: aldehyde, RCOR: ketone, RCOOH: carboxylic acid, RCOOR: ester, ROR: ether, RCCH: terminal alkyne, RCN: nitrile) among the Gcoupler-based *de novo* synthesized binders of Ste2p receptor across IC4 and IC5. **(d)** Box plots depicting the model's performances across the 10-fold cross-validation. The upper and lower box plots depict the performance metrics of models trained using the *de novo* ligands for

intracellular cavities (IC4 and IC5), respectively, of the Ste2 protein. **(e)** Venn diagrams depicting the number of yeast metabolites from YMDB predicted to bind to the Ste2p-Gpa1p interface, predicted using Gcoupler and AutoDock. Of note, IC4 and IC5 represent intracellular cavities 4 and 5 of the Ste2 protein, respectively. **(f)** Principal Component Analysis depicting chemical heterogeneity of endogenous yeast metabolites predicted to bind to the intracellular cavities (IC4 and IC5) of the Ste2 protein. Notably, the compounds were segregated into High-Affinity Metabolites (HAM) and Low-Affinity Metabolites (LAM) by the Generator module of the Gcoupler. **(g)** Heatmap illustrating the relative enrichment of the indicated functional groups among the endogenous intracellular allosteric modulators (metabolites) of Ste2 receptor across IC4 and IC5. **(h)** Percentage stacked barplot depicting the relative enrichment of the indicated functional groups of the High-Affinity Metabolites (HAM) and Low-Affinity Metabolites (LAM) across intracellular cavities (IC4 and IC5) of the Ste2 protein. **(i)** Heatmap depicting PageRank score of the selected metabolites for IC4 and **(j)** IC5 with respect to different biological properties. **(k)** Box plots depicting the performance parameters of the indicated models generated using Gcoupler against the IC4 cavity of Ste2p. Note the training and testing datasets were generated randomly (5 iterations) from the *in silico* synthesized ligands from Gcoupler. **(l)** Scatter plots depicting the segregation of High/Low-Affinity Metabolites (HAM/LAM) (indicated in green and red) identified using Gcoupler workflow with 100% training data. Of note, models trained on lesser training data size (25%, 50%, and 75% of HAB/LAB) severely failed to segregate High-Affinity Metabolites (HAM) and Low-Affinity Metabolites (LAM) (along Y-axis). X-axis represents the binding affinity calculated using IC4-specific docking using AutoDock. **(m)** Bar plots depicting the correlation values obtained between the Gcoupler prediction probabilities and AutoDock computed binding energies in the indicated training data size. **(n)** Box plots depicting the distributions for binding energies of the High-Affinity Metabolites and Low-Affinity Metabolites computed using cavity-specific docking and full docking via Autodock for IC4 and IC5 of the Ste2p.

Supplementary Figure 7: Untargeted metabolomics and genetic screening suggest an interlink between metabolites and Ste2p-mediated Programmed Cell Death.

(a) Screenshot of the central yeast metabolism from the Kyoto Encyclopedia of Genes and Genomes (KEGG) indicating the key metabolic pathways (highlighted in red) harboring metabolic intermediates predicted as high-affinity binders of GPCR-Gα-protein (Ste2p-Gpa1p) interface by Gcoupler. **(b)** Venn diagram depicting the percentage overlaps of the mating-related genes reported in the literature and those used in the screening. The *STE2* was the only common gene. **(c)** Heatmap depicting the growth curve profiles of the wild-type, single metabolic mutants, and *ste2Δ* under optimal growth conditions. **(d)** Schematic

diagram depicting the experimental workflow of the untargeted metabolomics experiment. Notably, the experiment involves the usage of increasing doses of α-factor to induce PCD and to enrich the surviving cells selectively. **(e)** Boxplot depicting the increase in the propidium iodide fluorescence upon the increasing concentration of α-factor treatment. Heat-killed (HK), untreated, and vehicle (DMSO-treated) were used as controls, whereas the increasing concentration of α-factor survived wild-type cells were used as test conditions. Mann Whitney U test was used to calculate statistical significance. Asterisks indicate statistical significance, whereas ns represents non-significance. **(f)** Heatmap depicting the relative (de)enrichment of differentially enriched metabolites in the indicated conditions. Of note, four biological replicates per condition were used in the untargeted metabolomics. **(g)** Principal Component Analysis depicting the segregation of indicated samples based on their metabolomics profiles along the PC1, PC2, and PC3. **(h)** Correlation plot depicting Pearson's correlation of the metabolome of the indicated samples. **(i)** Heatmap depicting the relative enrichment of all the detected metabolites in the indicated condition. Heat-killed (HK), untreated, and vehicle (DMSO-treated) were used as controls, whereas the increasing concentration of α-factor survived wild-type cells were used as test conditions. **(j)** Venn diagram indicating that 38 predicted intracellular allosteric modulators of Ste2p were identified in the untargeted metabolomics profiling. **(k)** Scatterplot depicting the Pathway Over Representation Analysis (ORA) results of the differentially enriched metabolites (treated vs. vehicle control) identified using untargeted metabolomics.

Supplementary Figure 8: Docking and Molecular Dynamics simulations suggest the stability of the Ste2-metabolite complex.

(a) Ligplots depicting the interacting amino acid residues and atoms of the Ste2 protein and indicated metabolites for the intracellular cavities (IC4 and IC5). **(b)** Table indicating the Van der Waals (ΔE_{vdw}), electrostatic (ΔE_{elec}), polar solvation (ΔE_{psolv}), and non-polar solvation (ΔE_{npsolv}) energies along with net binding free-energy (ΔG_{bind}) in kcal/mol of the three independent replicates of the indicated metabolites across intracellular cavities IC4 and IC5 of the Ste2p. Note the values in the table are provided as mean ± standard errors. **(c)** Line plot depicting the variation in the RMSD of the indicated metabolites bound to the intracellular cavity 4 (IC4) at the GPCR-Gα interface of the Ste2p, obtained using longer MD simulation runs. Notably, RMSD is provided in Angstroms (Å), whereas the simulation time is in nanoseconds (ns).

Supplementary Figure 9: Divergent characteristics of site-directed missense mutants of *STE2* gene.

(a) Line plots depicting the total energy decomposition of the individual amino acids of the Ste2p (three independent replicates) computed using MD simulations in IC4 (left) and IC5 (right). **(b)** Molecular representation of the Ste2 protein structures (blue) and the miniGpa1-proteins (cyan), with the highlighted interface residues (red and green) in the indicated conditions. **(c)** Scatterplot depicting the net binding free-energy ΔG (kcal/mol) of the Ste2p (with and without indicated metabolites) with miniG-protein (y-axis) and α-factor (x-axis). **(d)** Barplot depicting RMSD values of the Ste2 protein with indicated metabolite across intracellular cavities IC4 and IC5.

Supplementary Figure 10: Exogenous supplementation of selective metabolites rescues α-factor-mediated Programmed Cell Death.

(a) Growth curve profiles of the wild-type (control), *ste2Δ,* and wild-type yeast pre-treated with the indicated metabolites. **(b)** Schematic diagram (left) depicting the workflow opted to monitor α-factor-induced programmed cell death (PCD) in the wild-type yeast cells pre-loaded for 24 hours with ubiquinone 6 (CoQ6), zymosterol (ZST), and lanosterol (LST) at three different concentrations. Beanplots on the right depicting the changes in the α-factor-mediated PCD in the indicated conditions. Notably, cell viability was assessed by computing the area under the curve (AUC) of the growth kinetics. Mann Whitney U test was used to calculate statistical significance. Asterisks indicate statistical significance, whereas ns represents non-significance. **(c)** Beanplot depicting the fold change in the α-factor-mediated programmed cell death, assessed using the propidium iodide-mediated programmed cell death in the indicated conditions. Mann Whitney U test was used to calculate statistical significance. Asterisks indicate statistical significance, whereas ns represents non-significance. **(d)** Representative micrographs (left) depicting the growth of the cells (mating response) pretreated with indicated metabolites in the indicated single drop-out medium (SC-Lys and SC-Met). Quantifications of the mating response with respect to the SC-Met control are indicated as a bar graph (mean ± SEM) on the right (n = 3 biological replicates, each with three technical replicates). The Students' t-test was used to compute the statistical significance. Asterisks indicate statistical significance, whereas ns represents non-significance.

Supplementary Figure 11: Effects of Ste2 Mutants on Shmoo Formation in Response to α-Factor.

(a) Ligplots depicting the interacting amino acid residues of the mutant Ste2 proteins (mutation site indicated) and atoms of indicated metabolites at the intracellular cavities (IC4

and IC5). **(b)** Growth curve profiles of the reconstituted wild-type (rtWT), and indicated missense site-directed mutants. **(c)** Schematic representation depicting the overall experimental workflow designed for the quantitative assessment of the shmoos formation upon α-factor treatment. **(d)** Micrographs depicting the phase contrast images of the rtWT cells, pretreated with the indicated metabolites, with and without α-factor treatment, Scale 10 µm. Mean-Whisker plot (right) indicating the relative proportions of shmoos forming cells in the indicated conditions. **(e)** Micrographs depicting the phase contrast images of the indicated site-directed missense mutants of the *STE2* gene, pretreated with the indicated metabolites, with and without α-factor treatment, Scale 10 µm. Mean-Whisker plot (right) indicating the relative proportions of shmoos forming cells in the indicated conditions. The Students' t-test was used to compute the statistical significance of **d** and **e**. Asterisks indicate statistical significance, whereas ns represents non-significance. Error bars represent the standard error of the mean (SEM).

Supplementary Figure 12: RNA-Sequencing unveils genes involved in attenuating α-factor-induced cell death response.

(a) A table highlighting the key differentially expressed genes in the indicated conditions reported to be involved in regulating yeast mating response. Arrowheads and their direction represent the direction of differential expression. **(b)** A table highlighting the key differentially expressed genes in the indicated conditions reported to be involved in regulating yeast PCD-like signaling response. Arrowheads and their direction represent the direction of differential expression. **(c)** M-D plots (left) from the NOIseq analysis highlighting the differentially expressed genes (colored) in the indicated conditions. Bar plots (middle) depicting the prominent Gene Ontologies in the indicated conditions. Venn diagram (right) depicting the overlaps between the differentially expressed genes and the genes used in biochemical assays in this study. **(d)** Venn diagram depicting the overlap between the differentially expressed genes obtained from the RNA-Seq analysis and yeast knockout library. **(e)** Growth curve profiles of the wild-type and indicated knockouts from the yeast knockout library. **(f)** Box plot depicting the relative proportion of dead cells upon α-factor exposure in the indicated knockouts from the yeast knockout library as inferred using propidium iodide-based cell viability fluorometric assay (n=12 biological replicates from 2 experiments). The y-axis represents the fold change of the propidium iodide fluorescence values with respect to their respective controls. Mann Whitney U test was used to calculate statistical significance. Asterisks indicate statistical significance, whereas ns represents non-significance.

Supplementary Figure 13: Evolutionary Conservation of GPCR-Gα interface.

(a) Molecular representations depicting the topology of human and rat ADRB1 and ADRB2 receptors. GPCR-Gα interface cavities are color-coded at the intracellular sites. Of note, in the case of human ADRB1, the nomenclature of the two cavities detected at the interface includes 'Cv' (cavity) succeeded by the numerical number. **(b)** Barplots depicting the binding energies obtained by the docking of Human ADRB1 (7BVQ), Human ADRB2 (5X7D), Rat ADRB1 (P18090), and Rat ADRB2 (P10608) with the indicated metabolites at the GPCR-Gα interfaces. **(c)** Table depicting the conservation of yeast Ste2p-metabolite (ZST, CoQ6, and LST) interacting residues in the adrenergic receptors from humans and rats. **(d)** Schematic workflow illustrates the steps invloved in measuring and comparing the sequential and ligand-interaction conservation of GPCRs across six different species. **(e)** Donut charts illustrating the GPCR count across different species. **(f)** Phylogenetic tree representing 75 unique GPCRs from six species. **(g)** Empirical cumulative distribution function (ECDF) plot decpicting binding energy distribution of Gcoupler identified potential allosteric modulators along with five negative controls. **(h)** Heatmap depicting the pairwise d-values/p-values from the Kolmogorov-Smirnov statistical test under specified conditions. The lower triangle of the heatmap represents d-values, while the upper triangle shows p-values for the spcified pair. The test provides two key outputs: the D-value, which represents the maximum difference between the cumulative distribution functions (CDFs) of the two groups, and the p-value, which indicates the statistical significance of the observed difference. Symbols *, **, ***, and **** refer to p-values <0.05, <0.01, <0.001, and <0.0001, respectively.

SUPPLEMENTARY TABLES

Supplementary Table 1: Table contains information about the structure of the human GPCR-Gα-Protein complexes downloaded from the Protein Data Bank (PDB). It also contains information about the PDB IDs, Protein name, species information, whether it is used in this study or not, UniProt IDs, and other information.

Supplementary Table 2: The table contains information about the normalized Root Mean Square Deviation (RMSD) of the pairwise comparison of the GPCR-Gα-Protein interface (cavities) for the indicated GPCRs.

Supplementary Table 3: The table contains information about the chemical similarities of the *de novo* synthesized synthetic compounds of the indicated GPCR-Gα-Protein interface (cavities). Of note, the chemical similarity was computed using the Tanimoto coefficient on the Atomic fingerprints.

Supplementary Table 4: The table contains information about the YMDB metabolites predicted to bind at the intracellular cavities IC4 and IC5 of the Ste2 protein. Of note, predictions were made using molecular docking and Gcoupler. It contains information about the YMDB ID, Metabolite name, SMILES (Simplified Molecular Input Line Entry System), and cavities information. Of note, BE refers to binding energies, whereas probabilities were the outcome of Gcoupler.

Supplementary Table 5: The table contains information about the list of metabolite-gene pairs from the Kyoto Encyclopedia of Genes and Genomes (KEGG) pathway that is used in this study.

Supplementary Table 6: The table contains the results of the untargeted metabolomics. Of note, the values represent normalized and imputed peak intensities of the indicated metabolites.

Supplementary Table 7: The table contains the TMM normalized read counts after RNA Sequencing.

Supplementary Table 8: The table contains the list of Differentially Expressed Genes (DEGs) of the Control groups, alongside the other standard output from the NOISeq

analysis, such as M and D values, mean values of the two conditions, probability ranking, and other gene-associated features.

Supplementary Table 9: The table contains the list of Differentially Expressed Genes (DEGs) of the Control vs LST group, alongside the other standard output from the NOISeq analysis, such as M and D values, mean values of the two conditions, probability ranking, and other gene-associated features.

Supplementary Table 10: The table contains the list of Differentially Expressed Genes (DEGs) of the LST group, alongside the other standard output from the NOISeq analysis, such as M and D values, mean values of the two conditions, probability ranking, and other gene-associated features.

Supplementary Table 11: The table contains information about the comparison of *de novo* drug design and cavity detection tools. Please note, SBDD refers to Structure-Based Drug Design, and LBDD refers to Ligand-Based Drug Design.

Supplementary Table 12: The table contains information about the known mutants from the literature that could modulate Ste2 signaling. Of note, the table also contains information about the site of mutation, the nature of the mutation, its position within the intracellular cavities IC4 and IC5, their impact on the Ste2 signaling pathway, and references.

SUPPLEMENTARY INFORMATION

Supplementary Information

The supplementary Information provides details of the nucleotide and amino acid Multiple Sequence Alignments (MSAs) of the wild-type *STE2* and the site-directed missense mutants of *STE2*. Each row starts with the sequence identifier followed by the aligned sequence (in chunks) with the ending position of the aligned sequence provided at the end, separated by tabs. The mutation sites are highlighted in red (S75A), yellow (T155D) and blue (L289K). Supplementary Information also contains detailed materials and methods.

REFERENCES

1. D. Yang, *et al.*, G protein-coupled receptors: structure- and function-based drug discovery. *Signal Transduction and Targeted Therapy* **6**, 1–27 (2021).

2. K. Alhosaini, A. Azhar, A. Alonazi, F. Al-Zoghaibi, GPCRs: The most promiscuous druggable receptor of the mankind. *Saudi Pharmaceutical Journal* **29**, 539–551 (2021).

3. D. Calebiro, Z. Koszegi, Y. Lanoiselée, T. Miljus, S. O'Brien, G protein-coupled receptor-G protein interactions: a single-molecule perspective. *Physiol. Rev.* **101**, 857–906 (2021).

4. E. A. Wold, J. Zhou, GPCR Allosteric Modulators: Mechanistic Advantages and Therapeutic Applications. *Curr. Top. Med. Chem.* **18**, 2002–2006 (2018).

5. K. Bourque, *et al.*, Exploring the use of intracellular and extracellular allosteric modulators to understand GPCR signaling. *Allosteric Modulation of G Protein-Coupled Receptors* [Preprint] (2022). Available at: http://dx.doi.org/10.1016/b978-0-12-819771-4.00008-7.

6. S. Rees, D. Morrow, T. Kenakin, GPCR Drug Discovery Through the Exploitation of Allosteric Drug Binding Sites. *Receptors and Channels* [Preprint] (2002). Available at: http://dx.doi.org/10.3109/10606820214640.

7. K. Leach, P. M. Sexton, A. Christopoulos, Allosteric GPCR modulators: taking advantage of permissive receptor pharmacology. *Trends Pharmacol. Sci.* **28**, 382–389 (2007).

8. E. T. van der Westhuizen, C. Valant, P. M. Sexton, A. Christopoulos, Endogenous Allosteric Modulators of G Protein–Coupled Receptors. *J. Pharmacol. Exp. Ther.* **353**, 246–260 (2015).

9. M. Stornaiuolo, *et al.*, Endogenous vs Exogenous Allosteric Modulators in GPCRs: A dispute for shuttling CB1 among different membrane microenvironments. *Sci. Rep.* **5**, 15453 (2015).

10. D. Doller, Endogenous Allosteric Modulators of G Protein-Coupled Receptors: Implications in Drug Design. *2017 Medicinal Chemistry Reviews* [Preprint] (2017). Available at: http://dx.doi.org/10.29200/acsmedchemrev-v52.ch18.

11. A. Reyes-Alcaraz, E. Y. Lucero Garcia-Rojas, R. A. Bond, B. K. McConnell, Allosteric Modulators for GPCRs as a Therapeutic Alternative with High Potential in Drug Discovery. *Molecular Pharmacology* [Preprint] (2020). Available at: http://dx.doi.org/10.5772/intechopen.91838.

12. P. Zhang, L. Covic, A. Kuliopulos, Pepducins and Other Lipidated Peptides as Mechanistic Probes and Therapeutics. *Methods Mol. Biol.* **1324**, 191–203 (2015).

13. K. O'Callaghan, A. Kuliopulos, L. Covic, Turning receptors on and off with intracellular pepducins: new insights into G-protein-coupled receptor drug development. *J. Biol. Chem.* **287**, 12787–12796 (2012).

14. S. Basith, *et al.*, Exploring G Protein-Coupled Receptors (GPCRs) Ligand Space via Cheminformatics Approaches: Impact on Rational Drug Design. *Front. Pharmacol.* **9**, 128 (2018).

15. A. Gupta, *et al.*, Machine-OlF-Action: A unified framework for developing and interpreting machine-learning models for chemosensory research. *Bioinformatics* (2021). https://doi.org/10.1093/bioinformatics/btaa1104.

16. Y. Zhou, J. Meng, C. Xu, J. Liu, Multiple GPCR Functional Assays Based on Resonance Energy Transfer Sensors. *Front Cell Dev Biol* **9**, 611443 (2021).

17. C. Hoffmann, M. Bünemann, Fluorescence and Resonance Energy Transfer Shine New Light on GPCR Function. *GPCR Molecular Pharmacology and Drug Targeting* [Preprint] (2010). Available at: http://dx.doi.org/10.1002/9780470627327.ch10.

18. W. C. Jaeger, K. D. G. Pfleger, K. A. Eidne, Monitoring GPCR-Protein Complexes Using Bioluminescence Resonance Energy Transfer. *G Protein-Coupled Receptors* [Preprint]. Available at: http://dx.doi.org/10.1002/9780470749210.ch6.

19. M. Congreve, C. de Graaf, N. A. Swain, C. G. Tate, Impact of GPCR Structures on Drug Discovery. *Cell* **181**, 81–91 (2020).

20. S. Topiol, Current and Future Challenges in GPCR Drug Discovery. *Methods Mol. Biol.* **1705**, 1–21 (2018).

21. J. O. Spiegel, J. D. Durrant, AutoGrow4: an open-source genetic algorithm for de novo drug design and lead optimization. *J. Cheminform.* **12**, 25 (2020).

22. M. Sicho, X. Liu, D. Svozil, G. J. P. van Westen, GenUI: interactive and extensible open source software platform for de novo molecular generation and cheminformatics. *J. Cheminform.* **13**, 73 (2021).

23. Y. Li, J. Pei, L. Lai, Structure-based de novo drug design using 3D deep generative models. *Chem. Sci.* **12**, 13664–13675 (2021).

24. H. J. Böhm, The computer program LUDI: a new method for the de novo design of enzyme inhibitors. *J. Comput. Aided Mol. Des.* **6**, 61–78 (1992).

25. Y. Nishibata, A. Itai, Automatic creation of drug candidate structures based on receptor structure. Starting point for artificial lead generation. *Tetrahedron* **47**, 8985–8990 (1991).

26. D. A. Pearlman, M. A. Murcko, CONCEPTS: New dynamic algorithm forde novo drug suggestion. *J. Comput. Chem.* **14**, 1184–1193 (1993).

27. Y. Yuan, J. Pei, L. Lai, LigBuilder 2: a practical de novo drug design approach. *J. Chem. Inf. Model.* **51**, 1083–1091 (2011).

28. N.-N. Zhang, *et al.*, Multiple signaling pathways regulate yeast cell death during the response to mating pheromones. *Mol. Biol. Cell* **17**, 3409–3422 (2006).

29. S. S. Sokolov, K. V. Galkina, E. A. Litvinova, D. A. Knorre, F. F. Severin, The Role of LAM Genes in the Pheromone-Induced Cell Death of S. cerevisiae Yeast. *Biochemistry* **85**, 300–309 (2020).

30. M. Skalic, D. Sabbadin, B. Sattarov, S. Sciabola, G. De Fabritiis, From Target to Drug: Generative Modeling for the Multimodal Structure-Based Ligand Design. *Mol. Pharm.* **16**, 4282–4291 (2019).

31. M. Xu, T. Ran, H. Chen, De Novo Molecule Design Through the Molecular Generative Model Conditioned by 3D Information of Protein Binding Sites. *J. Chem. Inf. Model.* **61**, 3240–3254 (2021).

32. Y. Yuan, J. Pei, L. Lai, LigBuilder V3: A Multi-Target de novo Drug Design Approach. *Front Chem* **8**, 142 (2020).

33. O. Trott, A. J. Olson, AutoDock Vina: improving the speed and accuracy of docking with a new scoring function, efficient optimization, and multithreading. *J. Comput. Chem.* **31**, 455–461 (2010).

34. M. Bertoni, *et al.*, Bioactivity descriptors for uncharacterized chemical compounds. *Nat. Commun.* **12**, 3932 (2021).

35. M. M. Mysinger, M. Carchia, J. J. Irwin, B. K. Shoichet, Directory of useful decoys, enhanced (DUD-E): better ligands and decoys for better benchmarking. *J. Med. Chem.* **55**, 6582–6594 (2012).

36. S. Shen, *et al.*, Allosteric modulation of G protein-coupled receptor signaling. *Front. Endocrinol.* **14**, 1137604 (2023).

37. S. Nachtergaele, *et al.*, Oxysterols are allosteric activators of the oncoprotein Smoothened. *Nat. Chem. Biol.* **8**, 211–220 (2012).

38. J. B. Hedderich, *et al.*, The pocketome of G-protein-coupled receptors reveals previously untargeted allosteric sites. *Nat. Commun.* **13**, 2567 (2022).

39. A. Chatzigoulas, Z. Cournia, Rational design of allosteric modulators: Challenges and successes. *Wiley Interdiscip. Rev. Comput. Mol. Sci.* **11** (2021).

40. D. Bartuzi, A. A. Kaczor, D. Matosiuk, Opportunities and Challenges in the Discovery of Allosteric Modulators of GPCRs. *Methods Mol. Biol.* **1705**, 297–319 (2018).

41. T. Hou, Y. Bian, T. McGuire, X.-Q. Xie, Integrated Multi-Class Classification and Prediction of GPCR Allosteric Modulators by Machine Learning Intelligence. *Biomolecules* **11** (2021).

42. S. Topiol, New opportunities for GPCR allosteric modulators. *Future Medicinal Chemistry* [Preprint] (2018). Available at: http://dx.doi.org/10.4155/fmc-2017-0313.

43. W. Huang, *et al.*, Allosite: a method for predicting allosteric sites. *Bioinformatics* **29**, 2357–2359 (2013).

44. K. Song, *et al.*, Improved Method for the Identification and Validation of Allosteric Sites. *J. Chem. Inf. Model.* **57**, 2358–2363 (2017).

45. J. Zha, *et al.*, AlloReverse: multiscale understanding among hierarchical allosteric regulations. *Nucleic Acids Res.* **51**, W33–W38 (2023).

46. V. Le Guilloux, P. Schmidtke, P. Tuffery, Fpocket: an open source platform for ligand pocket detection. *BMC Bioinformatics* **10**, 168 (2009).

47. L. Shen, *et al.*, Pocket Crafter: a 3D generative modeling based workflow for the rapid generation of hit molecules in drug discovery. *J. Cheminform.* **16**, 33 (2024).

48. V. Velazhahan, *et al.*, Structure of the class D GPCR Ste2 dimer coupled to two G proteins. *Nature* **589**, 148–153 (2021).

49. C. G. Alvaro, J. Thorner, Heterotrimeric G Protein-coupled Receptor Signaling in Yeast Mating Pheromone Response. *J. Biol. Chem.* **291**, 7788–7795 (2016).

50. M. Bagnat, K. Simons, Cell surface polarization during yeast mating. *Proc. Natl. Acad. Sci. U. S. A.* **99**, 14183–14188 (2002).

51. H. Jin, J. M. McCaffery, E. Grote, Ergosterol promotes pheromone signaling and plasma membrane fusion in mating yeast. *J. Cell Biol.* **180**, 813–826 (2008).

52. A. Heese-Peck, *et al.*, Multiple functions of sterols in yeast endocytosis. *Mol. Biol. Cell* **13**, 2664–2680 (2002).

53. P. S. Aguilar, *et al.*, Structure of sterol aliphatic chains affects yeast cell shape and cell fusion during mating. *Proceedings of the National Academy of Sciences* **107**, 4170–4175 (2010).

54. C. Tiedje, D. G. Holland, U. Just, T. Höfken, Proteins involved in sterol synthesis interact with Ste20 and regulate cell polarity. *J. Cell Sci.* **120**, 3613–3624 (2007).

55. W. M. Shaw, *et al.*, Engineering a Model Cell for Rational Tuning of GPCR Signaling. *Cell* **177**, 782–796.e27 (2019).

56. N. Ostrov, *et al.*, A modular yeast biosensor for low-cost point-of-care pathogen detection. *Sci Adv* **3**, e1603221 (2017).

57. M. Clark, R. D. Cramer, N. Van Opdenbosch, Validation of the general purpose tripos 5.2 force field. *J. Comput. Chem.* **10**, 982–1012 (1989).

58. V. W. Berger, Y. Zhou, Kolmogorov–Smirnov Test: Overview. *Wiley StatsRef: Statistics Reference Online* [Preprint] (2014). Available at: https://onlinelibrary.wiley.com/doi/10.1002/9781118445112.stat06558.

59. S. Engmann, D. Cousineau, Comparing distributions: the two-sample Anderson-Darling test as an alternative to the Kolmogorov-Smirnoff test. *Journal of applied quantitative methods* **6** (2011).

60. S. J. Goerg, J. Kaiser, Nonparametric Testing of Distributions—the Epps–Singleton Two-Sample Test using the Empirical Characteristic Function. *Stata J.* **9**, 454–465 (2009).

61. G. Landrum, RDKit: A software suite for cheminformatics, computational chemistry, and predictive modeling. Available at: http://www.rdkit.org/RDKit_Overview.pdf [Accessed 11 August 2023].

62. B. Ramsundar, *et al.*, DeepChem: Democratizing Deep-Learning for Drug Discovery, Quantum Chemistry. *Materials Science and Biology. https://github. com/deepchem/deepchem (accessed Aug 8, 2017)* (2019).

63. T. N. Kipf, M. Welling, Semi-Supervised Classification with Graph Convolutional Networks. *arXiv [cs.LG]* (2016).

64. Z. Xiong, *et al.*, Pushing the Boundaries of Molecular Representation for Drug Discovery with the Graph Attention Mechanism. *J. Med. Chem.* **63**, 8749–8760 (2020).

65. P. Veličković, *et al.*, Graph Attention Networks. *https://openreview.net › forumhttps://openreview.net › forum* (2018).

66. A. Mittal, *et al.*, Artificial intelligence uncovers carcinogenic human metabolites. *Nat. Chem. Biol.* (2022). https://doi.org/10.1038/s41589-022-01110-7.

67. D. G. Gibson, *et al.*, Creation of a bacterial cell controlled by a chemically synthesized genome. *Science* **329**, 52–56 (2010).

68. D. G. Gibson, *et al.*, Enzymatic assembly of DNA molecules up to several hundred kilobases. *Nat. Methods* **6**, 343–345 (2009).

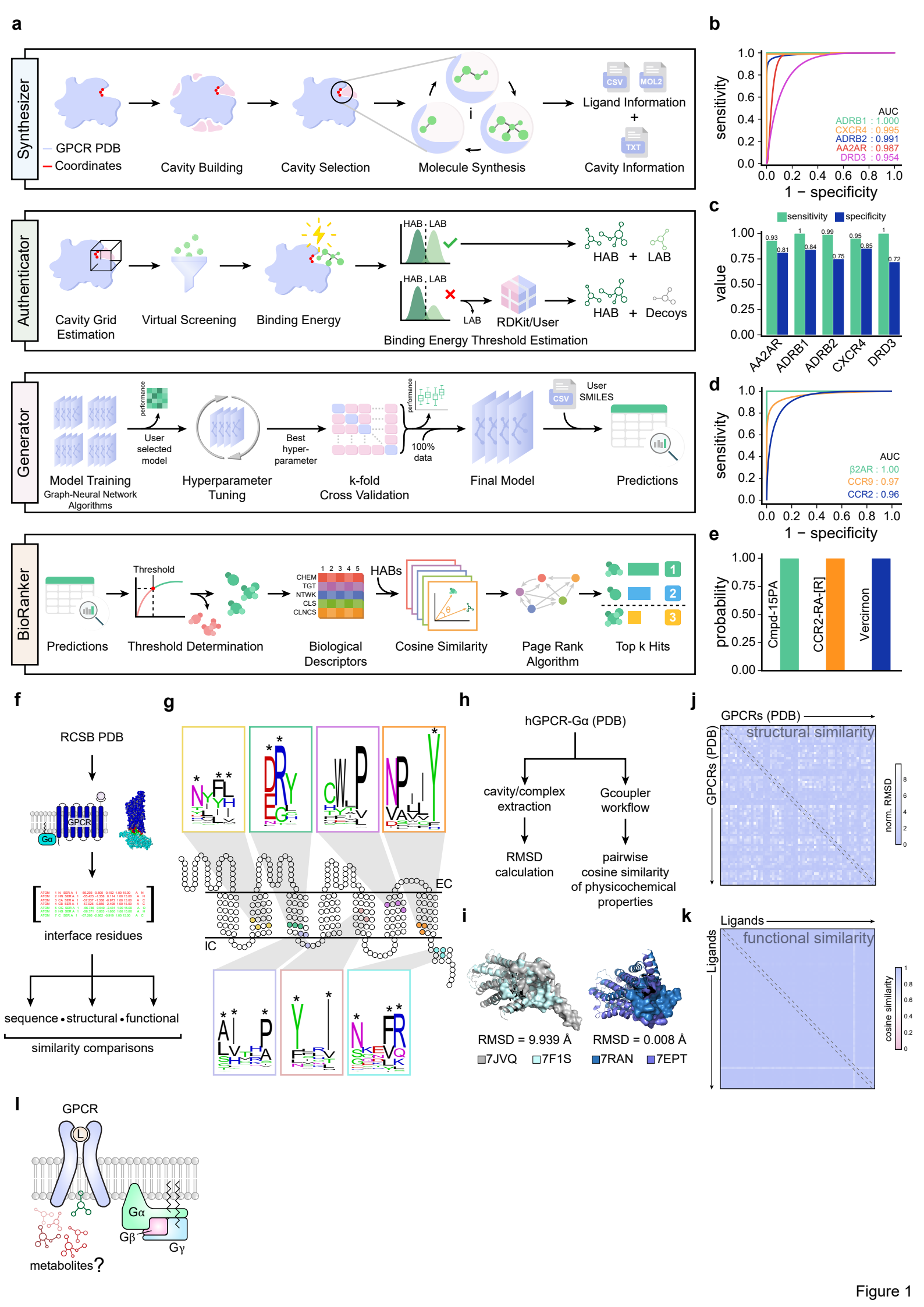
a
Synthesizer
GPCR PDB
Coordinates
Cavity Building
Cavity Selection
Molecule Synthesis
Ligand Information
+
Cavity Information
Authenticator
Cavity Grid Estimation
Virtual Screening
Binding Energy
HAB
LAB
HAB + LAB
HAB + Decoys
RDKit/User
Binding Energy Threshold Estimation
Generator
Model Training
Graph-Neural Network Algorithms
User selected model
Hyperparameter Tuning
Best hyper-parameter
k-fold Cross Validation
100% data
Final Model
User SMILES
Predictions
BioRanker
Predictions
Threshold
Threshold Determination
CHEM
TGT
NTWK
CLS
CLNCS
HABs
Biological Descriptors
Cosine Similarity
Page Rank Algorithm
Top k Hits
b
sensitivity
1 − specificity
AUC
ADRB1 : 1.000
CXCR4 : 0.995
ADRB2 : 0.991
AA2AR : 0.987
DRD3 : 0.954
c
sensitivity
specificity
value
AA2AR
ADRB1
ADRB2
CXCR4
DRD3
d
sensitivity
1 − specificity
AUC
β2AR : 1.00
CCR9 : 0.97
CCR2 : 0.96
e
probability
Cmpd-15PA
CCR2-RA-[R]
Vercirnon
f
RCSB PDB
GPCR
Gα
interface residues
sequence • structural • functional
similarity comparisons
g
EC
IC
h
hGPCR-Gα (PDB)
cavity/complex extraction
Gcoupler workflow
RMSD calculation
pairwise cosine similarity of physicochemical properties
i
RMSD = 9.939 Å
RMSD = 0.008 Å
7JVQ
7F1S
7RAN
7EPT
j
GPCRs (PDB)
structural similarity
norm. RMSD
k
Ligands
functional similarity
cosine similarity
l
GPCR
L
Gα
Gβ
Gγ
metabolites?

Figure 1

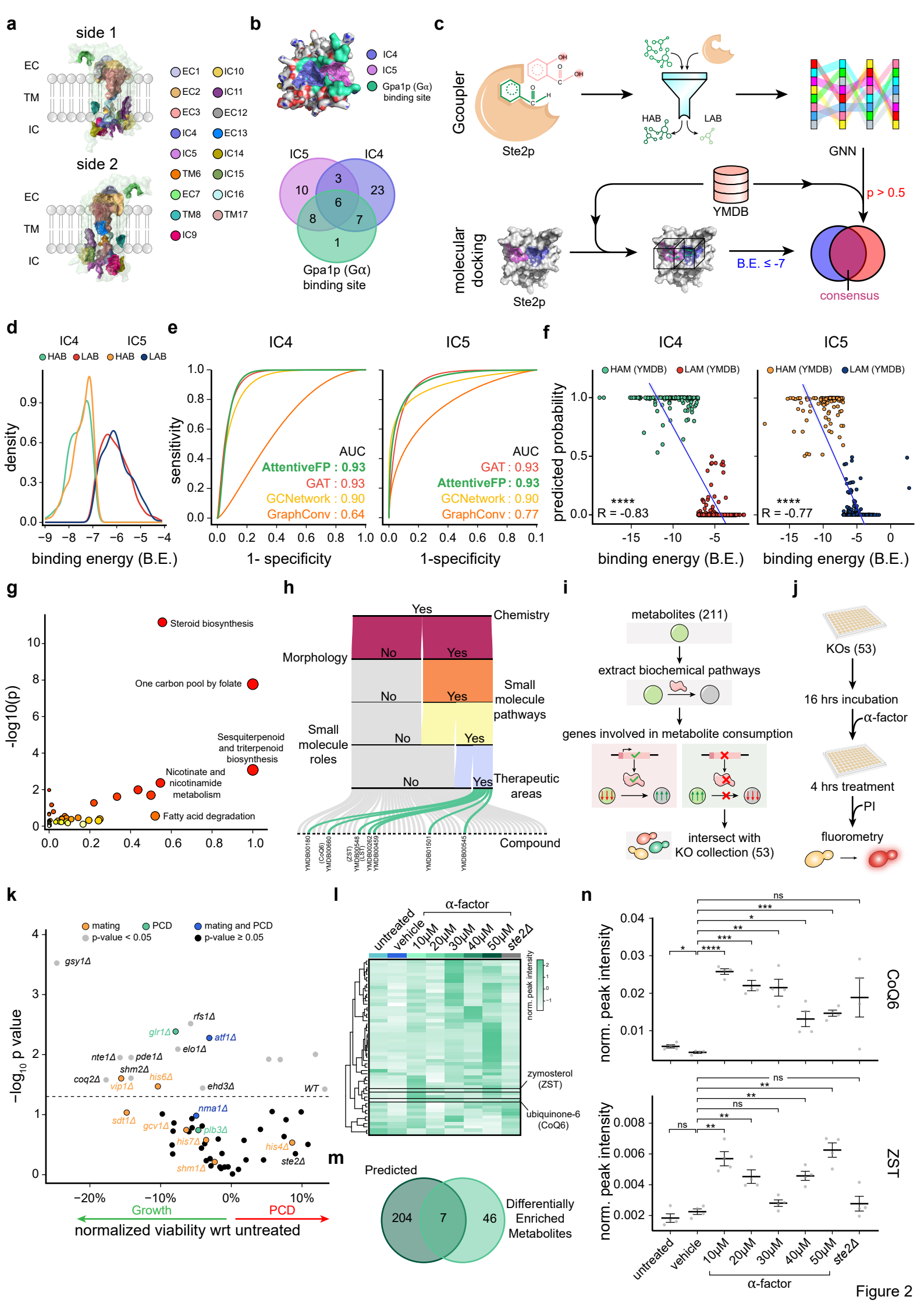
a
side 1
EC
TM
IC
side 2
EC1
EC2
EC3
IC4
IC5
TM6
EC7
TM8
IC9
IC10
IC11
EC12
EC13
IC14
IC15
IC16
TM17
b
IC4
IC5
Gpa1p (Gα) binding site
IC5
IC4
3
10
23
6
8
7
1
Gpa1p (Gα) binding site
c
Gcoupler
Ste2p
HAB
LAB
GNN
YMDB
p > 0.5
molecular docking
Ste2p
B.E. ≤ -7
consensus
d
IC4
IC5
HAB
LAB
HAB
LAB
density
binding energy (B.E.)
e
IC4
IC5
sensitivity
AUC
AttentiveFP : 0.93
GAT : 0.93
GCNetwork : 0.90
GraphConv : 0.64
AUC
GAT : 0.93
AttentiveFP : 0.93
GCNetwork : 0.90
GraphConv : 0.77
1- specificity
1-specificity
f
IC4
IC5
HAM (YMDB)
LAM (YMDB)
predicted probability
****
R = -0.83
****
R = -0.77
binding energy (B.E.)
binding energy (B.E.)
g
Steroid biosynthesis
One carbon pool by folate
Sesquiterpenoid and triterpenoid biosynthesis
Nicotinate and nicotinamide metabolism
Fatty acid degradation
-log10(p)
h
Yes
Chemistry
Morphology
No
Yes
No
Yes
Small molecule pathways
Small molecule roles
No
Yes
No
Yes
Therapeutic areas
Compound
i
metabolites (211)
extract biochemical pathways
genes involved in metabolite consumption
intersect with KO collection (53)
j
KOs (53)
16 hrs incubation
α-factor
4 hrs treatment
PI
fluorometry
k
mating
PCD
mating and PCD
p-value < 0.05
p-value ≥ 0.05
gsy1Δ
rfs1Δ
glr1Δ
atf1Δ
elo1Δ
nte1Δ
pde1Δ
shm2Δ
coq2Δ
his6Δ
vip1Δ
ehd3Δ
WT
nma1Δ
sdt1Δ
gcv1Δ
plb3Δ
his7Δ
his4Δ
ste2Δ
shm1Δ
−log10 p value
Growth
PCD
normalized viability wrt untreated
l
α-factor
untreated
vehicle
10μM
20μM
30μM
40μM
50μM
ste2Δ
norm. peak intensity
zymosterol (ZST)
ubiquinone-6 (CoQ6)
m
Predicted
204
7
46
Differentially Enriched Metabolites
n
norm. peak intensity
CoQ6
ZST
α-factor

Figure 2

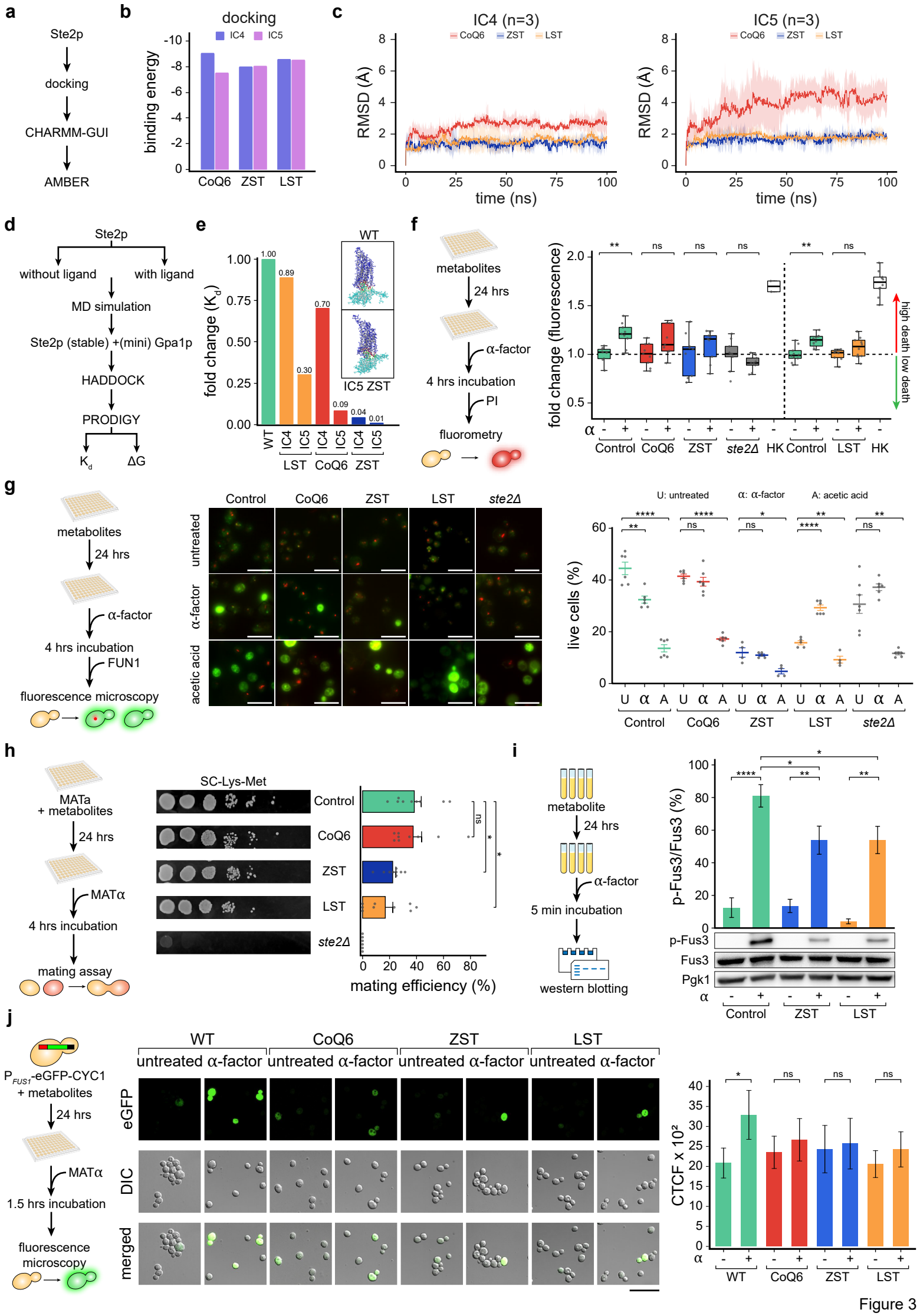
a
Ste2p
docking
CHARMM-GUI
AMBER
b
docking
IC4
IC5
binding energy
CoQ6
ZST
LST
c
IC4 (n=3)
IC5 (n=3)
CoQ6
ZST
LST
RMSD (Å)
time (ns)
d
Ste2p
without ligand
with ligand
MD simulation
Ste2p (stable) +(mini) Gpa1p
HADDOCK
PRODIGY
K_d
ΔG
e
fold change (K_d)
WT
IC5 ZST
LST
CoQ6
ZST
f
metabolites
24 hrs
α-factor
4 hrs incubation
PI
fluorometry
fold change (fluorescence)
high death
low death
Control
CoQ6
ZST
ste2Δ
HK
LST
g
metabolites
24 hrs
α-factor
4 hrs incubation
FUN1
fluorescence microscopy
untreated
α-factor
acetic acid
U: untreated
α: α-factor
A: acetic acid
live cells (%)
h
MATa
+ metabolites
24 hrs
MATα
4 hrs incubation
mating assay
SC-Lys-Met
mating efficiency (%)
i
metabolite
24 hrs
α-factor
5 min incubation
western blotting
p-Fus3/Fus3 (%)
p-Fus3
Fus3
Pgk1
j
P_FUS1-eGFP-CYC1
+ metabolites
24 hrs
MATα
1.5 hrs incubation
fluorescence microscopy
eGFP
DIC
merged
CTCF x 10²

Figure 3

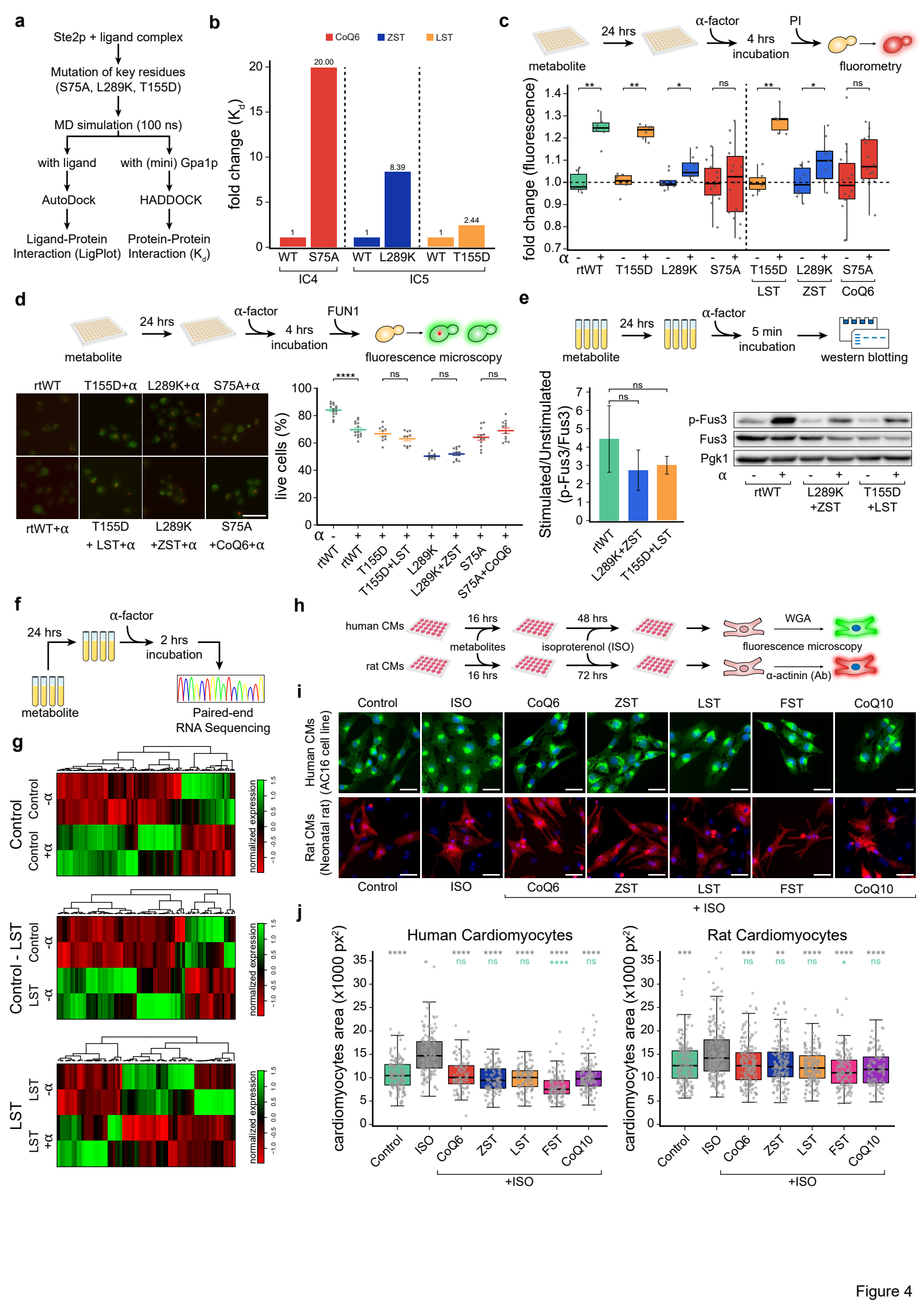
a
Ste2p + ligand complex
Mutation of key residues (S75A, L289K, T155D)
MD simulation (100 ns)
with ligand
with (mini) Gpa1p
AutoDock
HADDOCK
Ligand-Protein Interaction (LigPlot)
Protein-Protein Interaction (Kd)
b
CoQ6
ZST
LST
fold change (Kd)
20.00
8.39
2.44
WT
S75A
WT
L289K
WT
T155D
IC4
IC5
c
metabolite
24 hrs
α-factor
4 hrs incubation
PI
fluorometry
fold change (fluorescence)
rtWT
T155D
L289K
S75A
T155D
L289K
S75A
LST
ZST
CoQ6
d
metabolite
24 hrs
α-factor
4 hrs incubation
FUN1
fluorescence microscopy
rtWT
T155D+α
L289K+α
S75A+α
rtWT+α
T155D + LST+α
L289K +ZST+α
S75A +CoQ6+α
live cells (%)
rtWT
rtWT
T155D
T155D+LST
L289K
L289K+ZST
S75A
S75A+CoQ6
e
metabolite
24 hrs
α-factor
5 min incubation
western blotting
Stimulated/Unstimulated (p-Fus3/Fus3)
rtWT
L289K+ZST
T155D+LST
p-Fus3
Fus3
Pgk1
rtWT
L289K +ZST
T155D +LST
f
24 hrs
α-factor
2 hrs incubation
metabolite
Paired-end RNA Sequencing
g
Control
Control -α
Control +α
normalized expression
Control - LST
Control -α
LST -α
LST
LST -α
LST +α
h
human CMs
16 hrs
metabolites
48 hrs
isoproterenol (ISO)
WGA
fluorescence microscopy
rat CMs
16 hrs
72 hrs
α-actinin (Ab)
i
Control
ISO
CoQ6
ZST
LST
FST
CoQ10
Human CMs (AC16 cell line)
Rat CMs (Neonatal rat)
+ ISO
j
Human Cardiomyocytes
Rat Cardiomyocytes
cardiomyocytes area (x1000 px²)
+ISO

Figure 4